

# Doxorubicin Loaded Magnetic Polymersomes: Theranostic Nanocarriers for MR Imaging and Magneto-Chemotherapy

Charles Sanson,<sup>†,‡</sup> Odile Diou,<sup>†,‡</sup> Julie Thévenot,<sup>†,‡</sup> Emmanuel Ibarboure,<sup>†,‡</sup> Alain Soum,<sup>†,‡</sup> Annie Brûlet,<sup>§,⊥</sup> Sylvain Miraux,<sup>||, #</sup> Eric Thiaudière,<sup>||, #</sup> Sisareuth Tan,<sup>∇, ×</sup> Alain Brisson,<sup>∇, ×</sup> Vincent Dupuis,<sup>○, \*†</sup> Olivier Sandre,<sup>\*, †, ‡, ○, \*†</sup> and Sébastien Lecommandoux<sup>\*, †, ‡</sup>

<sup>†</sup>Université de Bordeaux/IPB, ENSCBP, 16 avenue Pey Berland, 33607 Pessac Cedex, France, <sup>‡</sup>CNRS, Laboratoire de Chimie des Polymères Organiques (UMR5629), Pessac, France, <sup>§</sup>CEA Saclay, LLB, 91191 Gif sur Yvette, France, <sup>⊥</sup>CNRS, Laboratoire Léon Brillouin (UMR12), Gif sur Yvette, France, <sup>||</sup>Université de Bordeaux, RMSB, 146 rue Léo Saignat, 33676 Bordeaux, France, <sup>#</sup>CNRS, Résonance Magnétique des Systèmes Biologiques (UMR5536), Bordeaux, France, <sup>∇</sup>Université de Bordeaux, IECB, 33402 Talence Cedex, France, <sup>×</sup>CNRS, Chimie et Biologie des Membranes et des Nanoobjets (UMR5248), Talence, France, <sup>○</sup>UPMC Université Paris 6, 4 place Jussieu, 75005 Paris, France, and <sup>\*</sup>CNRS, Physicochimie des Electrolytes, Colloïdes et Sciences Analytiques (UMR7195) Paris, France

Over the past decades, nanopolymeric therapeutics has proven to improve the effectiveness of cancer treatments in animal experiments.<sup>1–4</sup> During this period, progresses in modern polymer (physico)-chemistry have enabled the design of polymeric carriers with ever higher levels of complexity featuring addressable chemically reactive functions, defined chain architectures, and controlled morphologies and sizes. When applied to the field of drug delivery, these features allow achieving and combining several desirable properties such as high drug loading content, controlled release, increased circulation half-life and targeting of pathological areas or specific cell receptors. Polymer nanomedicines have the potential to increase the shelf life of chemotherapeutics before administration and to improve their efficacy after administration.<sup>5–7</sup> A direct consequence of the latter is the reduction in the dosing concentration and frequency of administration of the drug, hence the minimization of toxic side effects on healthy tissues, which are currently a major problem in chemotherapy. Among the different classes of polymeric nanomedicines, block copolymer vesicles also termed polymersomes offer an attractive structure for drug delivery applications.<sup>8–12</sup> This block copolymer self-assembly in a closed bilayer has fostered a considerable attention since both hydrophilic and hydrophobic drugs can be loaded either in the aqueous lumen or in the

**ABSTRACT** Hydrophobically modified maghemite ( $\gamma$ -Fe<sub>2</sub>O<sub>3</sub>) nanoparticles were encapsulated within the membrane of poly(trimethylene carbonate)-*b*-poly(L-glutamic acid) (PTMC-*b*-PGA) block copolymer vesicles using a nanoprecipitation process. This formation method gives simple access to highly magnetic nanoparticles (MNPs) (loaded up to 70 wt %) together with good control over the vesicles size (100–400 nm). The simultaneous loading of maghemite nanoparticles and doxorubicin was also achieved by nanoprecipitation. The deformation of the vesicle membrane under an applied magnetic field has been evidenced by small angle neutron scattering. These superparamagnetic hybrid self-assemblies display enhanced contrast properties that open potential applications for magnetic resonance imaging. They can also be guided in a magnetic field gradient. The feasibility of controlled drug release by radio frequency magnetic hyperthermia was demonstrated in the case of encapsulated doxorubicin molecules, showing the viability of the concept of magneto-chemotherapy. These magnetic polymersomes can be used as efficient multifunctional nanocarriers for combined therapy and imaging.

**KEYWORDS:** block copolymer vesicles · polymersome · nanoprecipitation · superparamagnetic iron oxide nanoparticles · maghemite · magnetic hyperthermia · magneto-chemotherapy · multifunctional · MRI contrast agent · doxorubicin · theranostics

membrane core respectively,<sup>13,14</sup> thanks to a thick membrane that imparts long-term stability to the object. After drug loading, vesicle disruption inducing drug release can be either triggered by an environmental stimulus, such as pH, temperature, light, or oxidation,<sup>15–17</sup> or can be the consequence of polymer hydrolytic or enzymatic degradation.<sup>18,19</sup> Even though a wide variety of polymer nanocarriers for drug delivery has shown efficient entrapment and controlled release of drugs *in vitro*, the evaluation of their biodistribution *in vivo* has become

\*Address correspondence to olivier.sandre@ipb.fr, lecommandoux@enscbp.fr.

Received for review October 14, 2010 and accepted December 24, 2010.

Published online January 10, 2011 10.1021/nn102762f

© 2011 American Chemical Society

possible by non invasive methods. To address this issue, one strategy consists in incorporating imaging probes together with the drugs into the polymer nanoparticles. These dual polymer nanocarriers for simultaneous cancer imaging and treatment open the field to “theranostic nanomedicines”, combining diagnostic and therapeutic components in an all-in-one nanoparticle.<sup>20,21</sup> Imaging probes to be loaded can belong to different families such as visible<sup>22,23</sup> and NIR fluorochromes,<sup>24</sup> radiotracers<sup>25–27</sup> or inorganic nanoparticles such as quantum dots,<sup>28–30</sup> gold nanoparticles,<sup>31–35</sup> or magnetic nanoparticles (MNPs).<sup>36,37</sup> Among the different MNPs, the so-called “ultrasmall superparamagnetic iron oxide” (USPIO) particles are synthetic  $\gamma$ -Fe<sub>2</sub>O<sub>3</sub> or Fe<sub>3</sub>O<sub>4</sub> nanometric grains in a perfectly dispersed state (*i.e.*, unclustered individual nanoparticles).<sup>38</sup> As described in numerous review articles,<sup>39–43</sup> iron oxide MNPs also called USPIOs are commonly used as negative contrast-enhancing agents in MRI, enabling high spatial resolution acquisition, three-dimensional, noninvasive imaging of the human body. Hydrophilic “stealth” polymers are often employed to enhance the stability and biocompatibility of the MNPs *in vivo* by hindering their further aggregation and by an antifouling effect against proteins of the immune system called opsonins.<sup>42,44</sup> Besides the MRI contrast enhancement properties attributed to their ability to distort strongly the magnetic field lines,<sup>45</sup> USPIOs can be used to kill cancer cells by their heating effect in radio frequency magnetic fields. Hyperthermia (or thermal ablation) is identified as a promising approach in cancer therapy, particularly in combination with chemo- or radio-therapy.<sup>41</sup> A promising hyperthermia route for treating deep tumors consists in concentrating MNPs around and inside the tumor site and increasing the temperature locally through conversion into heat of the energy from an external alternating magnetic field in the range of radio frequencies from 100 kHz to 1 MHz. This magnetic hyperthermia led to an intense research activity both on the optimization of the conditions of treatment (power, concentration, geometrical parameters, *etc.*)<sup>46–48</sup> and on the characteristics of the USPIOs themselves (chemical nature, distribution of sizes, *etc.*).<sup>39,49–57</sup>

For the purpose of obtaining multifunctional drug vectors, hydrophilic USPIOs have been loaded at first in the aqueous compartment of liposomes.<sup>58,59</sup> Under a permanent magnetic field, magnetic liposomes deform into elongated ellipsoids, as it was evidenced for giant unilamellar vesicles.<sup>60–62</sup> Interesting studies dealt with much smaller magneto-liposomes analogous in sizes to the pegylated lipid vectors of the DOXIL formulation of the anticancer drug doxorubicin hydrochloride (DOX). To combine magnetism and thermosensitivity, DOX was encapsulated into magnetic vesicles with a lipid membrane initially in the gel state and

becoming fluid at a temperature reachable by magnetic hyperthermia.<sup>63,64</sup> The application of a RF magnetic field led to massive release of encapsulated DOX since the magnetic hyperthermia was sufficient to reach locally the main chain phase transition temperature of the bilayer, thereby increasing the membrane permeability.<sup>65</sup> Recently, an analogous study with small hydrophobic USPIOs embedded in the membrane of liposomes evidenced the release triggered by a RF magnetic field of a fluorescent dye used as a model of hydrophilic drug.<sup>66</sup> The possibility to target a solid tumor by using magneto-liposomes and an extracorporeal magnet to guide them has also been reported.<sup>64,67,68</sup> Despite the tremendous results obtained with liposomes, the morphology of lipid/MNP systems strongly varies with MNP and lipid concentrations.<sup>69</sup> They also suffer from the classical issue of instability associated with lipid bilayers,<sup>70</sup> which incite to use of polymersomes as an alternative to liposomes. We have shown for the first time that hydrophobic USPIOs can be loaded into polymersome membranes of PB-*b*-PGA and that a reversible variation of the membrane thickness can be induced by the application of a magnetic field.<sup>71–73</sup> Later, Förster *et al.* induced the bridging of adjacent bilayers and formed multilamellar hybrid polymersomes by incorporating hydrophobic USPIOs into PI-*b*-PEO bilayers at a feed weight ratio up to 20% sufficiently large to guide the vesicles by a magnetic field gradient.<sup>74</sup>

In the present article, we describe a convenient procedure to prepare well-defined magnetic polymersomes featuring a hydrophobic internal membrane core made of the biodegradable block poly(trimethylene carbonate) (PTMC) and a polypeptide biocompatible corona of poly(L-glutamic acid) (PGA). Having synthesized USPIOs with the appropriate characteristics (size and hydrophobic coating), those were embedded together with the efficient antitumor drug doxorubicin hydrochloride (DOX) into the membrane of dual-loaded vesicles by one-step nanoprecipitation. This process allowed reaching quantitative loading contents and controlling the final sizes with low polydispersity. The two-dimensional confinement of USPIOs inside the vesicular membrane was evidenced by small angle neutron and light scattering techniques and observed by atomic force and transmission electron microscopy. The magnetic membrane of the PTMC-*b*-PGA polymersomes was shown to be reversibly deformable under a permanent magnetic field. The release of DOX under local hyperthermia conditions induced by an oscillating RF magnetic field was also evidenced as a proof of concept of magneto-chemotherapy with magnetic polymersomes.

## RESULTS AND DISCUSSION

**Characteristics of the USPIOs.** After synthesis,<sup>75</sup> size fractionation<sup>76</sup> and surfactant coating,<sup>77</sup> the radius of

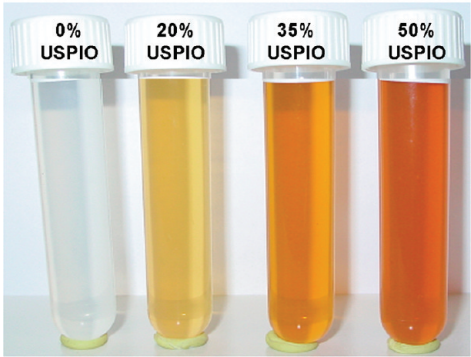
gyration and the hydrodynamic radius of the USPIO nanoparticles used in this work were  $R_G^{\text{USPIO}} = 3.05 \pm 0.06$  nm and  $R_H^{\text{USPIO}} = 4.7 \pm 0.07$  nm as measured respectively by SANS and DLS. The ratio  $R_G^{\text{USPIO}}/R_H^{\text{USPIO}} = 0.65$  is not far from the theoretical value 0.775 for dense spherical particles,<sup>78,79</sup> the gap being reasonably ascribed to the contribution of the surfactant layer to  $R_H^{\text{USPIO}}$  only. Those sizes are in good agreement with the distribution measured by VSM (Supporting Information, S-d),<sup>80,81</sup> described by a Log-normal law of median diameter  $D_{\text{mag}}^{\text{USPIO}} = 6.3$  nm, width  $\sigma = 0.22$  and weight averaged diameter  $D_w = 7.5$  nm. Concerning the magnetic hyperthermia capability, a specific loss power (SLP) of 14 W/g was reported for USPIOs synthesized by the same route and of analogous distribution of diameters ( $D_{\text{mag}}^{\text{USPIO}} = 6.7$  nm,  $\sigma = 0.20$ ,  $D_w = 7.7$  nm) but at larger frequency ( $f_{\text{RF}} = 700$  kHz) and much higher field intensity  $H_0$  (24.8 kA/m).<sup>54</sup> Using its expected variation with these parameters ( $\sim f_{\text{RF}} H_0^2$ ), we estimate a SLP value of 0.07 W/g in the conditions of biocompatible RF field used in this work ( $f_{\text{RF}} = 500$  kHz and  $H_0 = 2.12$  kA/m).

**Characteristics, Structure and Stability of USPIO-Loaded Vesicles.** In a previous study, the conditions of nanoprecipitation with the PTMC-*b*-PGA block copolymer were varied: choice of THF or DMSO as good solvent of the blocks, order (solvent into water or reverse) and duration of the addition.<sup>82</sup> The influence of each experimental parameter was rationalized in order to finely tune the sizes and PDI of the vesicles. In addition, the PTMC block was shown to be semicrystalline with an apparent melting temperature in vesicles near 34 °C (lower than that value at 37 °C in the bulk) that has a strong influence on the size of the vesicles and on their interactions.<sup>83</sup> In the present study, we checked that incorporating inorganic nanoparticles at the nanoprecipitation step did not affect the self-assembly process of the diblock copolymer and that vesicular morphologies were still obtained. The conditions were selected according to the low PDI obtained, the compatibility of the organic solvent and of the obtained vesicles' sizes with *in vivo* applications. The copolymer was first dissolved in DMSO with or without  $\gamma\text{-Fe}_2\text{O}_3$  USPIOs. Then water was added (up to 90% of the final volume) at a controlled flow rate to trigger self-assembly. As the flow rate strongly influences the final size of the vesicles,<sup>82</sup> we considered two sets of conditions: an almost instantaneous addition (5 s) leading to small vesicles ( $R_H = 45\text{--}67$  nm) denoted WDi and a 15 min-addition leading to larger ones ( $R_H = 187\text{--}202$  nm) denoted WD15. The characteristics of nanoparticles' dispersions prepared by either one or the other of these conditions at increasing USPIO feed weight ratios (FWR) are shown in Table 1.

The vesicles were found homogeneous in sizes, as observed by small PDI values in DLS. The loading of vesicles by USPIOs progressively increases the PDI (while remaining low) and slightly decreases  $R_H$ . This

**TABLE 1. Size and Polydispersity Index (PDI) of Nanoparticles' Dispersions Prepared with Increasing Feed Weight Ratios of USPIO Relative to Copolymer<sup>a</sup>**

WD15 vesicles



sample code	FWR (%)	$R_H$ (nm)	PDI
WDi-0	0	67	0.07
WDi-20	20	50	0.14
WDi-35	35	45	0.16
WDi-50	50	47	0.16
WDi-70	70	52	0.18
WD15-0	0	202	0.05
WD15-20	20	196	0.09
WD15-35	35	195	0.20
WD15-50	50	187	0.22

<sup>a</sup> Vesicles were prepared by nanoprecipitation in DMSO by adding water either in 5 s (WDi) or in 15 min (WD15). The image is a macroscopic view of samples.

hydrodynamic size decrease (more pronounced for WDi than for WD15) and slight broadening of the sizes' distribution (for both nanoprecipitation speeds) are ascribed to a larger hydrophobic effect when the copolymer is combined with USPIOs coated by surfactants, and thus to a larger driving force for a faster self-assembling process. No aggregation occurred below a critical USPIO FWR. Beyond this threshold value, the hydrophobic USPIOs began to aggregate during nanoprecipitation forming ill-defined macroscopic clusters that rapidly migrated to the vial walls when approaching a magnet. This maximum FWR was respectively 50 wt % for WD15 and 70 wt % for WDi. The larger threshold FWR with WDi vesicles compared to WD15 ones can be ascribed to a much faster kinetics of formation, thereby minimizing the probability of USPIOs' clustering before the completion of coassembly with the copolymer. The maximum loading content of USPIOs in the membrane of the WDi-70 vesicles corresponds to a local volume fraction  $\Phi_{\text{USPIO}}^{\text{mb}} = 12.1\%$ . Interestingly, this is close to the reported value of 11% for the insertion of USPIOs in bilayers of polystyrene-*b*-polyacrylate, whereas larger volume fractions, *e.g.*, 21% lead to a morphological transition into micelles *via* nanoparticles' clustering.<sup>84</sup> Fully dispersed and stable suspensions were observed below and up to these maximum USPIO FWR values. In these conditions, the shelf life is longer than several months at

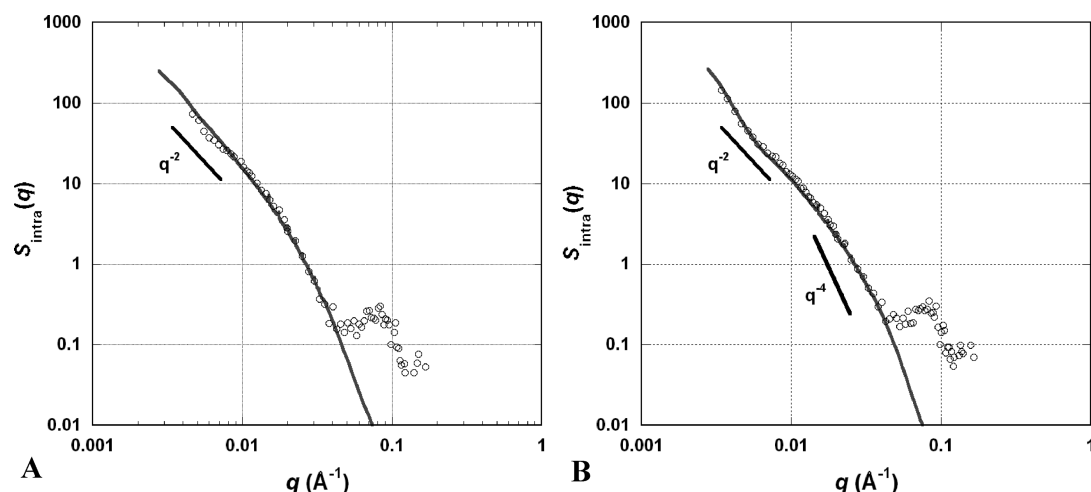


Figure 1. SANS curves of PTMC<sub>24</sub>-*b*-PGA<sub>19</sub> vesicles (A) WD15–50 and (B) WDi-70, centrifuged then dispersed at 10 mg/mL in a mixture H<sub>2</sub>O/D<sub>2</sub>O (65.6/34.4 v/v). Experimental intra-aggregate structure factors  $S_{\text{intra}}(q)$  of USPIOs are plotted as open circles. The solid lines represent the simulated form factors respectively for hollow spheres of mean radius (A)  $R = 130$  nm (PDI = 0.17) with membrane thickness  $\delta = 12$  nm (PDI = 0.3) for WD15–50 and (B)  $R = 45$  nm (PDI = 0.35) with  $\delta = 9$  nm (PDI = 0.3) for WDi-70.

room temperature. Static light scattering (SLS) measurements conducted on the WDi-50 sample strongly suggested a vesicular morphology. By drawing the Berry plot<sup>85</sup> over a scattering angular range from 50° to 150° and a concentration range from 0.2 to 1 mg/mL, we obtained the *z*-averaged radii of gyration ( $R_{G,z}$ ) allowing to calculate the ratio  $\rho = R_G/R_H$ . While vesicles are characterized by  $\rho$  values close to 1,  $\rho$  values around 0.775 are expected for spherical micelles.<sup>78,79</sup> WDi-50 suspensions had a  $\rho$  value of 1.02 in good agreement indeed with vesicular self-assemblies.

A further insight to the exact morphology of USPIO-loaded PTMC<sub>24</sub>-*b*-PGA<sub>19</sub> particles in either WDi or WD15 conditions was brought by small angle neutron scattering (SANS) experiments. Figure 1 represents the intra-aggregate structure factor  $S_{\text{intra}}(q)$  of the USPIOs measured by SANS in a solvent mixture matching the neutron scattering length density of the copolymer. The shape of  $S_{\text{intra}}(q)$  reflects both the interactions between the USPIOs inside the object and the overall shape of their aggregates in the attractive regime.<sup>86,87</sup> In the small *q*-regime,  $S_{\text{intra}}(q)$  followed a power law with a slope approximately  $-2$  typical of flat samples, supporting a vesicle-type morphology. In this *q*-region (Kratky–Porod regime), the thickness of the USPIO layer in the vesicle membrane can be calculated from the slope of  $\text{Ln}[q^2 \times S_{\text{intra}}(q)]$  plotted vs  $q^2$  which is  $-\delta^2/12$ .<sup>88</sup> From the experimental data, we obtained respectively  $\delta = 13$  nm and  $\delta = 10$  nm for samples WD15–50 and WDi-70. The vesicular membrane thus contains no more than one or two layers of magnetic colloids. More precisely, the data were properly fitted using a hollow sphere form factor with respectively an internal radius  $R = 130$  nm and shell thickness  $\delta = 12$  nm for WD15–50, and  $R = 45$  nm lumen radius with membrane thickness  $\delta = 9$  nm for WDi-70. These radii deduced from

SANS fits agree pretty well with the hydrodynamic radii in Table 1 measured by DLS. At large wave-vectors, the  $q^{-4}$  scaling law is typical of the Porod's regime expected for nanoparticles with a smooth interface. Moreover,  $S_{\text{intra}}(q)$  presents a correlation peak around  $8 \times 10^{-2} \text{ \AA}^{-1}$  (see Figure 1), associated to a most probable USPIO interparticle distance  $d_{\text{max}} = 2\pi/q_{\text{max}} = 7.8$  nm. Considering their weight-average diameter  $D_w = 7.5$  nm, we deduce that the USPIOs are closely packed inside the vesicular membrane for both WD15–50 and WDi-70 samples. The SANS curve of WDi-50 vesicles in D<sub>2</sub>O where the neutron scattering contrast of the USPIOs is almost matched also exhibits this correlation peak (Supporting Information S-c), as explained by the close-packed structure of holes in the copolymer membrane confining the USPIOs at a high local volume fraction.

To summarize our SANS results, we found membrane thicknesses equal to  $12.5 \pm 0.5$  nm and  $9.5 \pm 0.5$  nm (either by scaling law or by form factor fitting) for WD15–50 and WDi-70 vesicles respectively. Due to the chosen H<sub>2</sub>O/D<sub>2</sub>O solvent matching the copolymer scattering, these values represent the thickness of the USPIOs' layer only. In D<sub>2</sub>O solvent were the neutron scattering signal originates both from the magnetic contrast of iron oxide and the nuclear contrast of the copolymer, we measured a total membrane thickness  $29.1 \pm 0.6$  nm from Kratky–Porod's plots of the data reported in the ESI file (Supporting Information Figure S-c) for WDi vesicles independently of their iron oxide content (from 0 to 50% FWR), in accordance with the value  $30 \pm 2$  nm reported for the total membrane thickness of non magnetic vesicles made of PTMC<sub>24</sub>-*b*-PGA<sub>12</sub> with a similar PTMC block of molar mass  $M_n = 2750$  g/mol.<sup>82</sup> The measurement by SANS of the hydrophobic bilayer thickness for WDi vesicles well

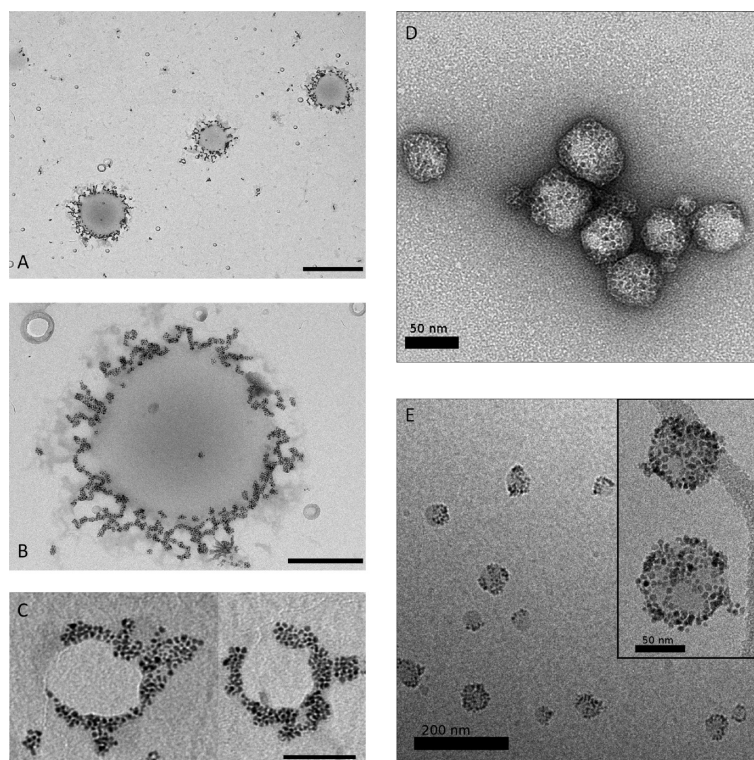


**Figure 2.** TEM images of USPIO-loaded vesicles prepared by nanoprecipitation. (A) Low magnification picture of WD15–50 vesicles (scale bar 1  $\mu\text{m}$ ). (B) Close-up view of a WD15–50 vesicle containing  $\sim 1500$  USPIOs as measured by image analysis (scale bar 300 nm). (C) WD1–70 vesicles spreading on the substrate, which enables counting  $\sim 190$  USPIOs on the left and  $\sim 220$  USPIOs on the right (scale bar 100 nm). (D) Image of negatively stained WD1–50 vesicles, showing a group of vesicles laying intact on the carbon substrate (scale bar 50 nm). (E) Cryo-TEM image showing homogeneously dispersed WD1–50 vesicles (scale bar 200 nm). (Inset) Close-up view of two vesicles showing a mantle of respectively  $\sim 80$  and  $\sim 110$  close-packed USPIOs with some uncovered areas (scale bar 50 nm).

compares to the value  $\delta = 9.6$  nm measured by cryo-TEM for polymersomes made of poly(ethylene oxide)-*b*-polybutadiene (noted EO<sub>26</sub>–BD<sub>46</sub> or OB2) with a total molar mass of 3600 g/mol and a hydrophilic fraction of 28%, thus a hydrophobic block mass of 2600 g/mol close to the one of PTMC here.<sup>70</sup> The 25% increase of hydrophobic thickness for WD15 vesicles is ascribed to the swelling of vesicles' membranes by the incorporation of USPIOs, which was presumably not possible for WD*i* ones due to their much higher curvature.

The WD15–50 and WD1–70 samples were further observed by TEM (Figure 2) and AFM (Figure 3) to confirm the vesicular morphology. TEM images mainly show the arrangement of the USPIOs because of the low electron scattering density of the copolymer compared to iron oxide. For both nanoprecipitation conditions (WD15 and WD*i*), hollow structures made of a close-packed arrangement of USPIOs were observed. The diameters measured on the TEM images 2B and 2C are around 750 and 150 nm respectively for WD15–50 and WD1–70 vesicles, which is larger than two times their hydrodynamic radii reported in Table 1 (374 and 104 nm respectively). This apparent discrepancy is ascribed to the total spreading of the vesicles onto the carbon substrate. The drying step during sample

preparation and the strong wetting on substrates presumably induced the rupture of membranes, which explains the presence of fragments as well as not entirely closed structures.<sup>71–73</sup> Unlike images A, B and C of Figure 2 that were obtained by spraying the samples onto the grids, image D originates from a more gentle protocol combined with staining (see Experimental) that led to vesicles sitting intact on the substrate. Both images D and E (cryoTEM) show apparent diameters much closer to the light scattering results, undoubtedly confirming the proposed structure. However we chose to show images A, B and C in spite of the spreading effect, because the flattening of the membrane onto the substrate enables to count the USPIOs per vesicle much easily than with the projection of intact spherical vesicles (D and E).

The WD*i* vesicles were also observed by AFM with and without the presence of 50 wt % USPIO. AFM phase images of empty vesicles (WD*i*-0) showed spherical vesicles, which aqueous interior leaked out due to drying and strong adsorption onto the freshly cleaved mica surface. When USPIOs were incorporated into the membrane (WD*i*-50), those presented multiple bright spots. The contrast of phase AFM pictures being proportional to the surface toughness,<sup>89,90</sup> we identify those bright spots with the hard inorganic USPIOs

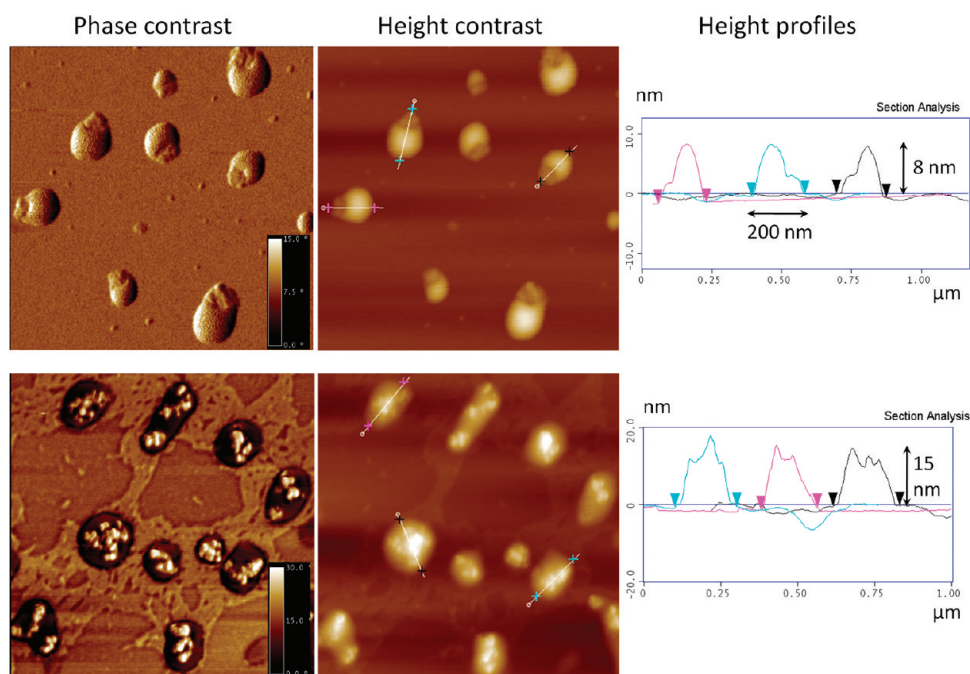


**Figure 3.** Tapping Mode AFM phase and height images of  $1 \times 1 \mu\text{m}$  surfaces of PTMC<sub>24</sub>-*b*-PGA<sub>19</sub> vesicles prepared by nanoprecipitation WDI without magnetic nanoparticles (upper panel) and with 50 wt % USPIO WDI-50 (lower panel). The average heights are measured on the right by cross sections.

embedded within the soft polymer matrix and spatially distributed over the vesicular surface as large patches. The average thicknesses of membranes spread on mica were analyzed on the AFM height images. These profiles revealed that the presence of USPIOs increase the thickness from 8 to 15 nm, the difference being very close to the weight average inorganic diameter  $D_w = 7.5$  nm. If the vesicles were adhering intact on the mica substrate, simply deflated by soft drying conditions, one would expect to measure an inorganic thickness equivalent to two layers of USPIOs (respectively from the top and the bottom of the closed membrane). But the AFM images correspond to a single membrane thickness instead, which indicates that the vesicles had burst and spread onto the substrate, as depicted schematically in Supporting Information S-h.

To conclude on the SANS, (cryo)TEM and AFM results, these measurements show that due to their hydrophobic coating, the USPIOs are confined in 2 dimensions within the membranes, between the two leaflets of the copolymer bilayer.

**Magnetization, Migration and Deformation under Magnetic Field of USPIO-Loaded Vesicles.** As for the magnetization properties, the magnetization curves of both individual USPIOs and USPIO-loaded vesicles were fitted according to Langevin's law of paramagnetism, each USPIO being a giant magnetic monodomain with an average magnetic dipole of  $8200 \mu_B$ , which is also the approximate number of  $\text{Fe}^{3+}$  ions per USPIO (see Supporting Information S-d). In Supporting Information Figure S-5, the VSM curve of WD15–50 vesicles loaded with 50 wt % USPIO exhibits a plateau value  $M_s/\Phi m_s$  allowing to

determine a concentration 0.43 g/L of USPIOs very close to the expected one (0.429 g/L, taking into account the USPIO FWR and the dilution effect during dialysis). Like previously stated, the vesicular dispersions were homogeneous, as attested by the detection of neither aggregates by DLS nor clusters of bare USPIOs moving when approaching a permanent magnet. Altogether, these results suggested a 100% loading efficiency for the USPIOs at feed weight ratios lower than 50% for WD15 and 70% for WDI vesicles.<sup>91</sup> Thus one can use mass conservation to deduce the values of the volume fraction  $\Phi$  of USPIOs inside the membranes, on the basis of their initial weight ratio (FWR) relatively to the copolymer and their respective mass densities  $d_{\text{USPIO}} = 5.1 \text{ g/cm}^3$  and  $d_{\text{copo}} = 1 \text{ g/cm}^3$ . An estimate of the mean number of USPIOs per vesicle of radius  $R_H$  and membrane thickness  $\delta$  can be calculated according to:

$$N_{\text{USPIO}}^{\text{vesicle}} = \frac{V_{\text{mb}} \times \Phi_{\text{mb}}^{\text{USPIO}}}{V_{\text{USPIO}}} \quad (1)$$

where the volume of membrane is calculated by  $V_{\text{mb}} = 4\pi R_H^2 \delta$  using geometrical values obtained by DLS and SANS respectively and  $V_{\text{USPIO}}$  is averaged over the size distribution law of diameters ( $\pi D_w^3/6$ ). These calculations for each set of experiments gathered in Table 2 lead to estimated numbers of USPIOs in pretty good accordance with the values observed on the TEM pictures of Figure 2.

The migration of the WD15–50 vesicles under a controlled magnetic field gradient was also used to estimate differently the number of confined USPIOs

averaged on a large population of vesicles. The assessment of the ability of magnetic polymersomes to be attracted and concentrated at a specific location *in vivo* is also particularly relevant. Compared to magnetophoresis experiments with objects of sizes around 10  $\mu\text{m}$  such as giant liposomes or biological cells,<sup>62,92–95</sup> a supplemental difficulty arose from the low value of the Peclet's hydrodynamic number, which means that the magnetophoretic motion of the vesicles was not significantly larger than their Brownian motion (see the videos supplied as Supporting Information). Usually, magnetophoretic measurements with such colloidal particles prone to thermal agitation are done by measuring light absorption profiles as a function of time and space.<sup>96–99</sup> In the present work, we chose alternatively a statistical method to infer the average drift velocity  $V_{\text{drift}}$  and the diffusion constant  $D_{\text{vesicle}}$  by following a large number of individual trajectories, as once described in a study of Brownian colloids in a liquid crystal (Figure 47).<sup>100</sup>

The Brownian motion appears isotropic with a unique translation diffusion constant  $D_{\text{ves}} = 1.11 \mu\text{m}^2/\text{s}$ . The Stokes–Einstein's formula gives a hydrodynamic

radius deduced by video-microscopy  $R_{\text{H}}^{\text{video}} = 196 \text{ nm}$  comparable to the value obtained by DLS. Due to an imperfect alignment of the magnetic field gradient with the  $x$  axis, we had to extract both coordinates of the magnetophoretic motion to calculate the total drift velocity:

$$\|\vec{V}_{\text{drift}}\| = \sqrt{V_x^2 + V_y^2} = 1.09 \mu\text{m}/\text{s} \quad (2)$$

This experimental value is compared to the theoretical estimate obtained by balancing the forces acting on a spherical magnetic vesicle at steady state in an external magnetic field gradient, which are the magnetophoretic force  $F_{\text{B}}$ , and the viscous drag,  $F_{\text{v}}$ , acting against it. The two forces are given by:

$$F_{\text{B}} = m \frac{dB}{dz} \quad (3)$$

and

$$F_{\text{v}} = 6\pi\eta R_{\text{H}} V_{\text{drift}} \quad (4)$$

where  $m$  is the magnetic moment of the vesicle,<sup>101</sup>  $dB/dz$  is the gradient of the magnetic field,  $\eta$  is the viscosity of the solvent,  $R_{\text{H}}$  is the hydrodynamic radius of the vesicle, and  $V_{\text{drift}}$  is the velocity of the particle. From the exact balance of the magnetic and the viscous forces, we calculate a theoretical magnetophoretic velocity  $V_{\text{drift}} \approx 0.5 \mu\text{m}/\text{s}$  for the WD15–50 vesicles under a field gradient  $dB/dz = 18.5 \text{ T}/\text{m}$ . The factor around one-half between the expected drift velocity and the value  $V_{\text{drift}} = 1.09 \mu\text{m}/\text{s}$  measured experimentally cannot be ascribed to the statistical noise because the uncertainties of the average displacements were estimated at 0.4 and 1.6% for the histograms at  $\tau$  and  $2\tau$  time steps containing respectively 64 519 and 3920 data points. As a tentative explanation, we know from a reported work on giant

**TABLE 2. Characteristics of USPIO-Loaded Vesicles<sup>a</sup>**

sample code	USPIO FWR (%)	$\Phi_{\text{USPIO}}^{\text{mb}}$ (%)	$R_{\text{H}}$ (nm)	$N_{\text{USPIO}}^{\text{vesicle}}$
WD15–20	20	3.8	196	1085
WD15–35	35	6.4	195	1830
WD15–50	50	8.9	187	2340
WDi-20	20	3.8	50	55
WDi-35	35	6.4	45	75
WDi-50	50	8.9	47	110
WDi-70	70	12.1	52	190

<sup>a</sup> Feed weight ratio, hydrodynamic radius  $R_{\text{H}}$ , local volume fraction  $\Phi$  of USPIOs in membrane and their number  $N$  per vesicle calculated by eq 1 with respectively  $\delta = 13 \text{ nm}$  for WD15 samples and  $\delta = 10 \text{ nm}$  for WDi ones (SANS values).

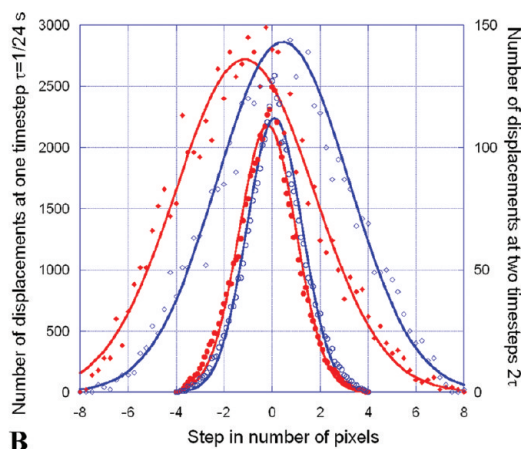
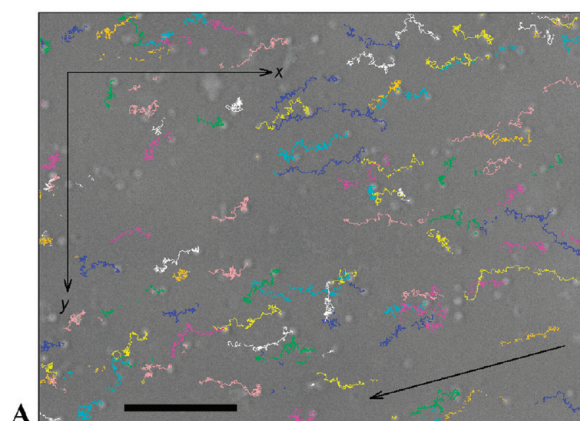


**Figure 4.** Video microscopy snapshot (inverted bright field image) superposed with the trajectories (A) during 10s of WD15 PTMC<sub>24</sub>-b-PGA<sub>19</sub> vesicles loaded with 50 wt % of USPIOs. The vesicles were discriminated from the background by image analysis with the ParticleTracker plugin for ImageJ. The magnetophoretic mobility of the vesicles is visualized by the shifts between the histograms (B) of displacements in the  $x$  (red markers) and the  $y$  (blue markers) directions for durations respectively of  $\tau = 1/24 = 0.042 \text{ s}$  (circles) and  $2\tau$  (diamonds). The arrow indicates the direction of magnetic field gradient of intensity  $dB/dz = 18.5 \text{ T}/\text{m}$ . The scale bar represents  $20 \mu\text{m}$ .

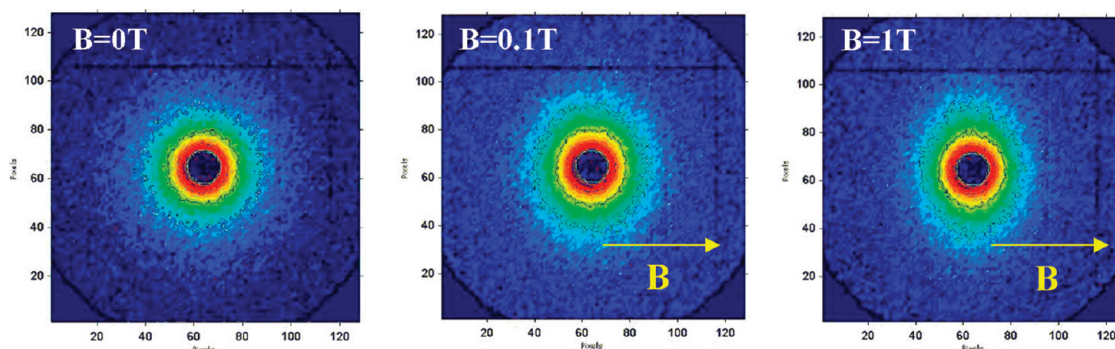


**Figure 5.** Anisotropic SANS patterns of WD15–50 in H<sub>2</sub>O in the  $q$  range  $3 \times 10^{-3} - 3 \times 10^{-2} \text{ \AA}^{-1}$  under a magnetic field (horizontal) of intensity  $B = 0 \text{ T}$  (left),  $B = 0.1 \text{ T}$  (middle) and  $B = 1 \text{ T}$  (right). Each color corresponds to an iso-intensity range.

magnetic liposomes that the drag coefficient is enhanced compared to Stokes' formula if the vesicles were deformed by the field into high aspect ratio ellipsoids during their migration.<sup>102</sup> Another correction compared to the drag coefficient of a solid sphere originates also from the viscous dissipation inside the fluid magnetic membrane, for instance if it was subjected to a “caterpillar” or a “crawling” motion.<sup>103</sup> In addition to these pure hydrodynamic effects, the measured  $V_{\text{drift}}$  higher than its expected value might be explained by an underestimate of the numbers of USPIOs per vesicle appearing in Table 2. This would occur for example in the case of a non negligible amount of “blank vesicles” that were undetected but increased the average LC of iron oxide inside the magnetic vesicles above the USPIO/copolymer ratio (FWR) used for nanoprecipitation.

Apart from estimating the magnetic payload of the vesicles, the magnetophoresis experiment is also relevant to estimate their efficiency for magnetic guiding both *in vivo* and *in vitro*. Their magnetophoretic mobility in the vicinity of a strong NdFeB magnet is indeed of the same order of magnitude than values  $\sim 1 \mu\text{m/s}$  reported by studies that evidenced the enhanced uptake of magnetic nanocarriers by cell cultures under field gradients.<sup>104,105</sup> For *in vivo* experiments, it was hypothesized that the accumulation of magnetic colloids injected in the main bloodstream at a specific region under magnetic field requires that their migration is faster than the blood velocity in the smallest vessels alimending the tumor.<sup>98</sup> However, the guiding of magnetic stealth liposomes injected in the caudal vein of mice by a strong permanent magnet applied directly on a solid tumor was evidenced, even though their drift velocity was  $10 \mu\text{m/s}$  only.<sup>68</sup> A model experiment consisting in attracting clusters of MNPs of submicrometer diameters (330 nm) by a permanent magnet while they were circulating in a flow loop showed that they were efficiently deposited at the surface of the capillary near the magnet even with a stream velocity as high as  $1 \text{ cm/s}$ .<sup>106</sup> Therefore we believe that the USPIO loaded vesicles WD15–35 or WD15–50 are good candidates for such magnetic

targeting applications, whereas the WDi vesicles might be too small and contain an insufficient number of USPIOs.

The magnetic response of PTMC<sub>24</sub>-*b*-PGA<sub>19</sub> vesicles with their membrane filled by 50 wt % (WD15–50) or 70 wt % USPIO (WDi-70) was also studied by anisotropic SANS under an applied magnetic field. Vesicles were dispersed in light water (H<sub>2</sub>O) in order to work in almost pure nuclear contrast conditions under field. The magnetic contrast of the  $\gamma\text{-Fe}_2\text{O}_3$  USPIOs in H<sub>2</sub>O being much lower than the nuclear contrast, the anisotropy of the SANS signal was not simply due to magnetization but reflects the spatial organization of the USPIOs and their possible rearrangement under magnetic field. The SANS patterns of WD15–50 vesicles are shown in Figure 5 at increasing field intensities up to 1 T.

The scattering patterns became clearly anisotropic when a magnetic field was applied to the sample. The lines of iso-intensity in the  $3 \times 10^{-3}$  to  $3 \times 10^{-2} \text{ \AA}^{-1}$   $q$ -range were elliptical, elongated perpendicularly to the field direction. One possible scenario compatible with this asymmetry consists in the deformation of the hollow spheres formed by the USPIOs into either oblate or prolate ellipsoids symmetric by rotation along the field direction. However, one should keep in mind that the observed  $q$ -range corresponds to the length scale of the membrane thickness rather than to the whole size and shape of the vesicles.<sup>71–73</sup>

In order to study this shape anisotropy more quantitatively, the scattering patterns were averaged in angular sectors around two directions parallel ( $^{\parallel}$ ) and perpendicular ( $^{\perp}$ ) to the magnetic field. Examples of the resulting intensity curves are plotted in Figure S-2 (Supporting Information S-b). By comparing the difference  $q^{\perp} - q^{\parallel}$  in these two directions relatively to the wave vector  $q^0$  obtained by an isotropic averaging at the same intensity value, an anisotropy factor could be calculated for each sample and each magnetic field intensity (Table 3).

The calculated anisotropy factors confirmed the increase of membrane anisotropy with the applied magnetic field already visible on the SANS patterns.



The anisotropy factor increased mainly between 0.1 and 0.6 T for both vesicular dispersions and remained almost constant up to 1 T. The plateau value reached at 0.6 T is ascribed to the saturation of the magnetic moment of a vesicle above  $B \approx 0.7$  T as observed on the magnetization curve (Supporting Information Figure S-5). It is worth noticing that the anisotropy parameter is smaller for WDi-70 than for WD15–50 vesicles, as explained by the number of USPIOs per vesicle (12 times smaller for WDi-70 than for WD15–50) and by the vesicle size (4 times smaller). Presumably due to their smaller size associated with a higher membrane curvature, WDi-70 vesicles are less prone to magnetic deformation than the much larger WD15–50 ones.

**USPIO-Loaded Vesicles as Contrast Agents for MRI.** The efficiency of MRI contrast agents based on USPIO is usually assessed by measuring the  $T_1$  (longitudinal) and  $T_2$  (transverse) relaxation times of the proton spins relaxations. Then the relaxation rates  $1/T_1$  and  $1/T_2$  are plotted versus total iron concentration in mM and the resulting slopes ( $s^{-1}mM^{-1}$ ) called respectively  $r_1$  and  $r_2$  relaxivities can be used to compare different samples of USPIO differing by their size, dispersity, local concentration, aggregation state or any other parameter like the confinement in either a hydrophilic or a hydrophobic environment. In particular the encapsulation of USPIOs in hydrophobic polymers hampers the diffusion of water protons in the vicinity of USPIOs, which results in poor  $T_1$  contrast enhancement,<sup>107</sup> so that we can infer the same effect in our systems where the USPIOs are buried within a hydrophobic membrane. In addition,  $r_1$  decreases rapidly as a function of the applied magnetic field (*i.e.*, the Larmor's resonance frequency) while  $r_2$  reaches a plateau value due to the so-called "secular term" in its theoretical expression.<sup>45,108</sup>

**TABLE 3. Anisotropy Factor of WD15–50 and WDi-70 Vesicles Calculated from Anisotropic Averaging of their SANS Patterns at 6  $cm^{-1}$  iso-Intensity under Increasing Magnetic Field Intensities**

$B$ (T)	$(q^{\perp} - q^{\parallel})/q^0$ (%)	
	WD15–50	WDi-70
0.1	11.3	6.8
0.6	24.4	12.7
1	26.8	12.0

**TABLE 4. Longitudinal ( $r_1$ ) and Transverse ( $r_2$ ) Relaxivities of USPIO-Loaded WDi Vesicles when Used as Contrast Agents for MRI at 4.7 T, Deduced from the Linear Fits of the Relaxation Rates  $1/T_1$  and  $1/T_2$  versus Molar Concentrations Both of Ferric Ions (in mM) or of Vesicles (in nM)<sup>a</sup>**

sample code	$R_H$ (nm)	$N_{Fe^{3+}}^{vesicle}$	$r_{1 Fe^{3+} \text{ ion}}$ ( $s^{-1}mM^{-1}$ )	$r_{1 vesicle}$ ( $s^{-1}nM^{-1}$ )	$r_{2 Fe^{3+} \text{ ion}}$ ( $s^{-1}mM^{-1}$ )	$r_{2 vesicle}$ ( $s^{-1}nM^{-1}$ )
WDi-20	50	$4.5 \times 10^5$	$2.8 \pm 0.02$	$1.3 \pm 0.01$	$81 \pm 1$	$37 \pm 0.4$
WDi-35	45	$6.2 \times 10^5$	$3.6 \pm 0.08$	$2.2 \pm 0.05$	$134 \pm 2$	$83 \pm 1.2$
WDi-50	47	$9.0 \times 10^5$	$3.6 \pm 0.2$	$3.3 \pm 0.2$	$173 \pm 7$	$156 \pm 6$
WDi-70	52	$1.6 \times 10^6$	$3.5 \pm 0.1$	$5.5 \pm 0.2$	$182 \pm 4$	$283 \pm 7$

<sup>a</sup> Number of  $Fe^{3+}$  per vesicle is the product of the number of USPIOs per vesicle (Table 2) by 8200  $Fe^{3+}$  per USPIO on average.

The  $T_1$  and  $T_2$  relaxation times were measured on a 4.7 T (200MHz) research MRI system. Their inverse values  $1/T_1$  and  $1/T_2$  were plotted as a function of iron molar concentration for PTMC-*b*-PGA vesicles prepared in WDi condition with USPIOs' FWR ranging from 20 to 70 wt %. The  $r_1$  and  $r_2$  relaxivities deduced from the slopes are reported in Table 4. To assess the experimental sensitivity, the solutions were diluted by a factor from 20 to 500: no vesicle size variation was observed by DLS under such dilutions. While  $r_1$  values are weak and almost constant ( $\sim 3 s^{-1}mM^{-1}$ ),  $r_2$  values are of the same order of magnitude ( $\sim 100 s^{-1}mM^{-1}$ ) and even larger than for commercial  $T_2$  contrast agents: these are either individual (AMI-227, Ferumoxtran/Sinerem)<sup>109</sup> or clustered (AMI-25, Feridex/Endorem)<sup>110,111</sup> USPIOs coated with a Dextran polymer, the latter being denominated SPIOs because of their larger size. The clustering of USPIOs inside objects at a high loading density is indeed known to enhance the negative contrast for  $T_2$ -sequence MRI images compared to individual USPIOs, as reported for hydrophobic USPIOs in micelles<sup>107,112,113</sup> or hydrophilic ones in liposomes<sup>114</sup> or electrostatic coacervates with charged polymers.<sup>115</sup> However, the articles that link the experimental  $r_2$  values to theory are rather scarce: they dealt with SPIOs made of magnetite cores aggregated by Dextran of varying sizes<sup>116</sup> and more recently with individual USPIOs coated by a controlled thickness of silica.<sup>117</sup> In the present work, we note a steeper slope in Figure 6A for WDi-35 ( $r_2 = 134 \pm 2 s^{-1}mM^{-1}$ ) as compared to WDi-20 ( $r_2 = 81 \pm 1 s^{-1}mM^{-1}$ ). These relaxivities are both larger than the value  $r_2 = 39 \pm 2 s^{-1}mM^{-1}$  reported for USPIOs individually dispersed in water synthesized by the same aqueous route and of the same size distribution.<sup>115</sup> For 50 wt % USPIOs in the vesicles, the transverse relaxivity reached  $r_2 = 173 \pm 7 s^{-1}mM^{-1}$ , but then it saturates near this value at  $r_2 = 182 \pm 4 s^{-1}mM^{-1}$  for the highest loading content 70 wt %. On the theoretical point, A. Roch *et al.* predicted such a plateau of  $r_2$  when increasing the size of clusters of USPIOs.<sup>116</sup>

To evidence the effect of USPIO-loaded vesicles on  $T_2$ -weighted MR images, Figure 6B shows MR images of wells containing increasing concentrations of WDi-70 vesicles. A remarkable darkening (*i.e.*, negative contrast

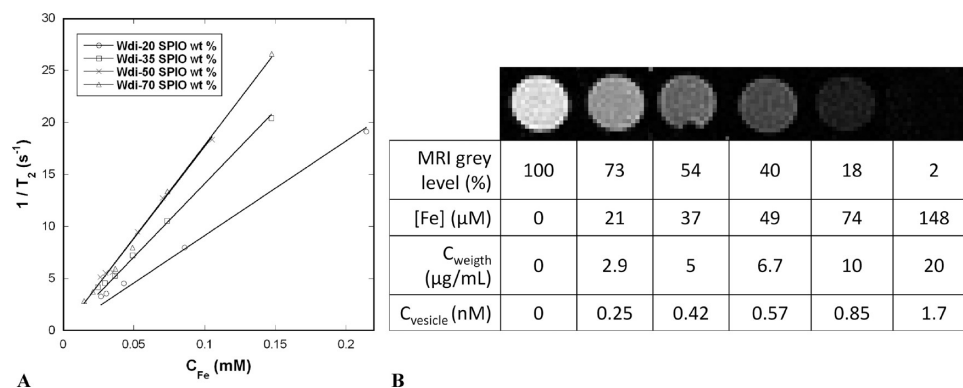


**Figure 6.** (A) Transverse relaxation rates ( $1/T_2$ ,  $\text{s}^{-1}$ ) as a function of iron concentration (mM) for PTMC<sub>24</sub>-*b*-PGA<sub>19</sub> vesicles (WDi) loaded with 20, 35, 50, and 70 USPIO wt %. The slopes give the  $r_2$  value, respectively  $81 \pm 1$ ,  $134 \pm 2$ ,  $173 \pm 7$  and  $182 \pm 4$   $\text{s}^{-1}\text{mM}^{-1}$ . (B)  $T_2$ -weighted MRI images extracted from  $T_2$  measurements experiment (4.7 T; multiple spin-echo 2D imaging sequence;  $T_R = 10000$  ms; inter echo-time, 5 ms; number of echo images, 256; FOV,  $50 \times 50$  mm; matrix,  $128 \times 128$ ; slice thickness, 1 mm) of WDi-70 vesicles at different dilution factors. The table gives the molar concentrations of iron ions, the total weight concentrations and the equivalent molar concentrations of vesicles.

enhancement) appeared even at low vesicle concentration. The MRI detection limit, defined as the copolymer concentration at which the MRI signal intensity decreases to 50% of that of pure water,<sup>107</sup> was measured at  $6.7 \mu\text{g/mL}$  for WDi-70 vesicles. Since the molar mass of the vesicles measured by SLS is  $1.182 \times 10^7$  g/mol (Supporting Information S-i), the above sensitivity limit corresponds to a vesicle concentration of approximately 0.5 nM, which is 1 order of magnitude lower than the 5 nM reported for magnetic micelles<sup>107</sup> and, to our knowledge, the lowest value ever reported. For applications such as the evaluation of the biodistribution or the targeting efficiency of a drug conveyed in nanocarriers, the concentration of ferric ions may not be the most relevant parameter for the radiologists. Therefore the  $r_1$  and  $r_2$  relaxivities are also expressed in Table 4 according to the concentration of vesicles in nM to facilitate the comparison with other nanoparticulate contrast agents. Unlike the relaxivities per ferric ion which saturate, their values per WDi vesicle increase monotonously with the magnetic FWR inside the membrane, at an almost constant hydrodynamic size.

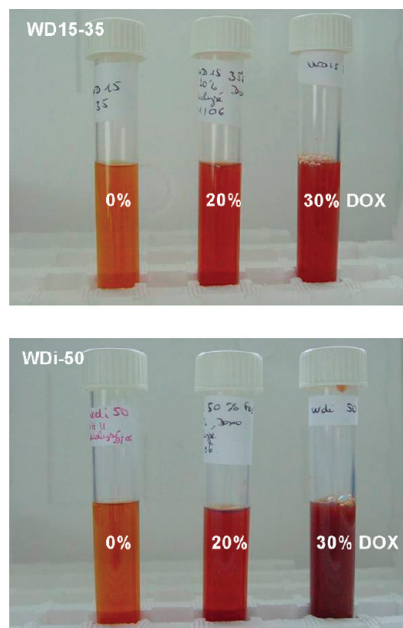
#### Doxorubicin Loading and Release by Macroscopic Heating.

To determine the feasibility of magnetically controlled drug release, a dual loading of USPIOs and of doxorubicin was carried out. The nanoprecipitation was performed at pH 10.5 in order to deprotonate the DOX ( $\text{p}K_a \approx 8.3$ ), thus maximizing the loading content (LC = 34% without size variation at 50% FWR) and extending the release duration as described in a previous work.<sup>118</sup> For each vesicular dispersion, the USPIO feed weight ratio (FWR) was fixed at a value lower than the maximum USPIO loading (namely 50 wt % for WDi and 35 wt % for WD15) so that space was left in the membrane for DOX entrapment. The DOX FWR in the nanoprecipitation mixture was then progressively increased. A DOX FWR of 20% was selected for both vesicular types since a drug loading at this level did not

alter the self-assembly of the vesicles significantly: Table 5 shows indeed a moderate variation of their hydrodynamic size ( $R_H$  decreases by 16% for WD15 and increases by 8% for WDi) and an unchanged surface charge. A larger 30% DOX FWR can be sustained by WD-15 vesicles without any size change, but for the smaller WDi-50 vesicles it leads to a 2-fold size increase, presumably due to their larger curvature energy already invoked to explain their lower deformability under static magnetic field.

After nanoprecipitation with dual-loading in DOX and USPIOs, an extensive dialysis against a large volume (4 L) of Tris buffer (pH 7.4, 30 °C, ionic strength 150 mM) during 4 h allowed to reduce the pH back to 7.4 and to completely remove the unbound drug and DMSO. As for the colloidal stability of these dual loaded vesicles, their  $\zeta$  potential remained strongly negative ( $\sim -40$  mV). Therefore the corona of PGA chains was unaffected, which excludes the precipitation of the USPIOs and of the drug onto the hydrophilic chains and proves their embedment deeply inside the vesicular PTMC-*b*-PGA membrane. The loading content (LC) and loading efficiency (LE) of DOX were determined by spectrophotometry. Values obtained for both vesicular dispersions with or without USPIOs are gathered in Table 6. A DOX LC around 10 wt % was found in all cases, independently of the presence of USPIOs in the membrane. Finally, the colloidal stability of the WDi vesicles was tested in MEM cell culture medium with fetal bovine serum (10% v/v FBS), and no change in size was observed for 24 h.

Comparing precisely the DOX loading efficiency between dual loaded vesicles and non magnetic ones, we observe that LE decreases by 22% for WD15 vesicles, whereas it increases by 22.5% for WDi ones. As a result, the insertion of USPIOs and DOX appears competitive in the case of the larger WD15 vesicles, certainly due to a lack of space in the membrane (the difference between  $\Phi_{\text{mb}}^{\text{USPIO}}$  and its maximal value

**TABLE 5.** Doxorubicin Feed Weight Ratio (FWR), Hydrodynamic Size, Polydispersity Index and  $\zeta$  Potential of WD15-35 and WDi-50 Vesicles<sup>a</sup>

sample code	DOX FWR (%)	$R_h$ (nm)	PDI	$\zeta$ (mV)
WD15-35	0	152	0.15	-39.6
	20	124	0.23	-39.3
	30	128	0.16	nd <sup>b</sup>
WDi-50	0	56.5	0.22	-40.8
	20	61	0.15	-42.0
	30	137	0.20	nd <sup>b</sup>

<sup>a</sup> The pictures show the corresponding sample tubes. <sup>b</sup> Not determined.

**TABLE 6.** Influence of USPIO Feed Weight Ratio (FWR) on the DOX Loading Content and Efficiency into WDi and WD15 Vesicles<sup>a</sup>

sample code	USPIO FWR (%)	DOX FWR (%)	DOX LC (%)	DOX LE (%)
WD15	0	20	12.5	74
	35	20	9	52
WDi	0	20	9.5	47.5
	50	20	12	70

<sup>a</sup> FWR is in wt % relatively to copolymer in DMSO before nanoprecipitation. The LC is measured by spectrophotometry after nanoprecipitation and dialysis. The LE is the yield LC/FWR.

being only 2.5%, see Table 2). On the opposite, the incorporation seems cooperative for the smaller WDi vesicles. Such synergetic effect of dual loading has already been mentioned for copolymer micelles, for which the LC of DOX could be enhanced from 3 to 12 wt % by the coencapsulation with hydrophobic USPIOs.<sup>36</sup>

Subsequently, *in vitro* release studies from the several prepared vesicular dispersions were monitored in various conditions by comparing the absorbance at  $\lambda_{\max} = 485$  nm with the DOX absorbance calibration

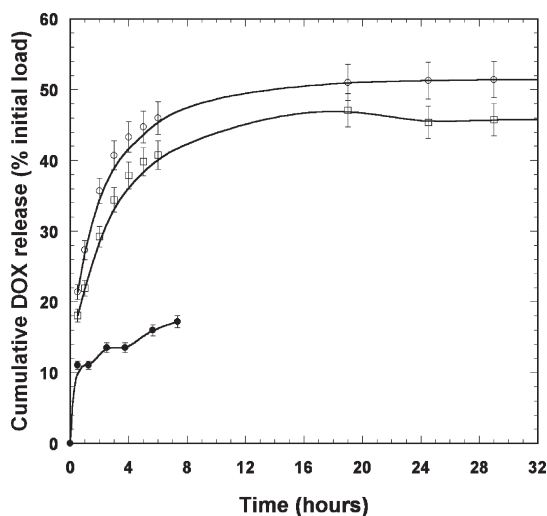


**Figure 7.** *In vitro* release kinetic profiles of USPIO/DOX dual loaded vesicles with initial 20% DOX FWR obtained for WDi-50 (○) and WD15-35 (□) vesicles at 37 °C and for WDi-50 vesicles at 23 °C (●). In all cases, the release medium was Tris 10 mM (pH 7.4, ionic strength 150 mM).

curve (after background correction). The release kinetics *in vitro* at 37 °C of WDi-50 and WD15-35 vesicles fed with 20 wt % DOX appear almost similar. As seen in Figure 7, indeed, a plateau at around 50 wt % of released DOX was reached in both cases after one day. As stated in a previous work on the physicochemical conditions to optimize the loading and release of DOX with PTMC-*b*-PGA vesicles (but for a DOX LC of 34 wt % 3 times larger than in the present work and without USPIOs),<sup>118</sup> temperature has a strong influence on the kinetics as well as on the amount of drug released: the plateau values at 5 °C, 20 °C, 37 and 45 °C were found respectively equal to 5%, 30%, 60% and 85% of the initial DOX load in the vesicles. This temperature sensitivity is presumably due to the semicrystalline nature of the PTMC blocks inside membranes evidenced once by microcalorimetry<sup>83</sup> and in this work by birefringence measurement (see Supporting Information S-e).

In Figure 7, only 15% of DOX was released after 6 h at 23 °C compared to 45% released after the same time at 37 °C thus above the melting temperature of PTMC in the membrane of vesicles.

**Doxorubicin Release by Magnetic Hyperthermia.** Having in mind this thermo-sensitivity of the release rate of DOX *in vitro* from dual-loaded PTMC-*b*-PGA vesicles, we studied the effect of an excitation by an oscillating magnetic field of the USPIOs confined in the membranes. Submitted to a strong radio frequency field, USPIOs are known to dissipate heat originating from friction losses of their magnetic dipoles according to two different relaxation modes: Néel's relaxation consisting in the flips of each dipole between the "easy axes" of the crystalline structure and the Brownian rotational diffusion of the USPIO grains in the solvent of viscosity  $\eta$ . According to a commonly accepted

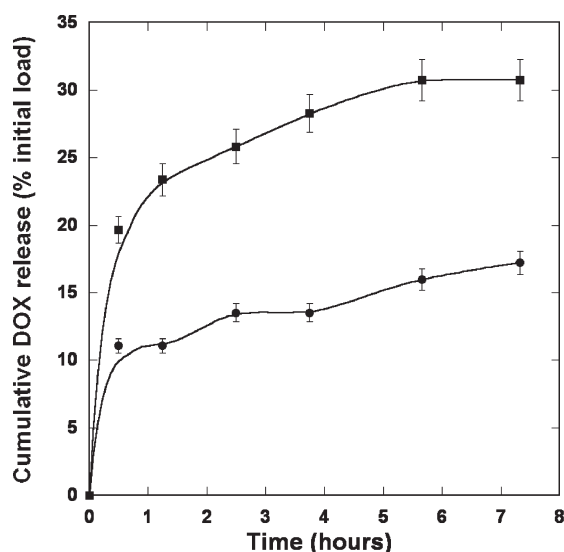


**Figure 8.** Influence of a RF oscillating magnetic field on the *in vitro* release kinetics of WDi-50 vesicles at constant bath temperature (23 °C); ●,  $B = 0$  T; ■, AC magnetic field ( $f_{\text{RF}} = 500$  kHz,  $B_0 = 2.65$  mT).

model,<sup>50</sup> the specific loss power under a field of frequency  $f_{\text{RF}}$  and mean intensity  $H_0$  expressed in W/g writes:

$$\text{SLP}(f_{\text{RF}}, H_0) = \frac{\pi f_{\text{RF}}}{d} \chi''(f_{\text{RF}}) H_0^2 \text{ with}$$

$$\chi''(f_{\text{RF}}) = \mu_0 \frac{m_S^2 V_{\text{USPIO}}}{3k_B T} \frac{2\pi f_{\text{RF}} \tau_{\text{eff}}}{1 + (2\pi f_{\text{RF}} \tau_{\text{eff}})^2} \quad (5)$$

Here  $\chi''(f_{\text{RF}})$  is the loss term of the dynamic susceptibility of an USPIO with specific magnetization  $m_S$ , mass density  $d$  and volume  $V_{\text{USPIO}}$ . The effective relaxation time  $\tau_{\text{eff}}$  corresponds to the fastest mode between the two mechanisms participating to thermal dissipation. Both of them can be expressed as functions of the particle volume:

$$\tau_{\text{Néel}} = \tau_0 \times \exp(K_a V_{\text{USPIO}} / k_B T) \quad (6)$$

with  $\tau_0 \approx 10^{-9}$  s and  $K_a \approx 10^4$  J/m and

$$\tau_{\text{Brown}} = 3\eta V_{\text{USPIO}} / k_B T \quad (7)$$

Although it does not take into account the possible variation of relaxation times with the magnetic field intensity,<sup>119</sup> this model correctly describes the strong dependence of the *SLP* with the size distribution of a suspension of USPIOs<sup>53</sup> and gives an optimal diameter about 14–15 nm. When USPIOs are confined in a viscous environment as in lipid membrane compartments inside biological cells (endosomes), the Brownian relaxation mode can be neglected.<sup>54,120</sup>

Figure 8 displays the kinetic profiles at constant temperature 23 °C with and without the application of an oscillating magnetic field of frequency  $f_{\text{RF}} = 500$  kHz and mean field intensity  $H_0 = 2.12$  kAm<sup>-1</sup>. Although these field conditions might appear weak, they were already over passing by more than a factor two the

upper dose of RF irradiation  $f_{\text{RF}} \times H_0 < 4.85 \times 10^8$  Am<sup>-1</sup>s<sup>-1</sup> recommended for a human being.<sup>121</sup> After 7 h, the DOX release content is multiplied by a factor 2 under RF field compared to the same vesicles with USPIOs embedded in the membrane but kept away from the coil. The heat produced *via* Néel's relaxation is believed to increase the fluidity of the semicrystalline polymeric membrane, increasing dramatically the diffusion of the encapsulated DOX out of the membrane. It should be stressed that we have not observed any macroscopic heating of the vesicular dispersion.<sup>122</sup> Even if the global temperature of the suspension remained almost unchanged, we infer that a local temperature raise around 7 °C took place in the close vicinity of the membrane (*i.e.*, at the nanometric scale). The approximately 2-fold enhancement of DOX release rate under the RF magnetic field (Figure 8) was indeed of the same type than the 3-fold enhancement observed when the vesicular suspension was heated macroscopically by 14 °C thus above the melting temperature of the PTMC blocks (Figure 7). A control experiment performed by placing the WDi-50 vesicles during several hours under a constant magnetic field of intensity  $B_0 = 0.4$  T showed that a static deformation of the vesicles had no impact on the release rate of DOX, thereby confirming the necessity to excite the USPIOs at a frequency in the RF-range close to their Néel's relaxation in order to detect an effect on the membrane permeability of the vesicles.

## CONCLUSIONS

In the present study, the formation of new hybrid vesicular self-assemblies from the biodegradable PTMC-*b*-PGA copolymer and hydrophobically coated  $\gamma$ -Fe<sub>2</sub>O<sub>3</sub> nanoparticles has been investigated. Hybrid vesicles have been obtained by one-step nanoprecipitation, leading to high loading content of magnetic nanoparticles (up to 70 wt %) in the membrane together with a good control over vesicles' size and dispersity. The vesicular morphology was elucidated by combining light and neutron scattering techniques together with electronic and atomic force microscopy. These magnetic vesicles exhibited a long-term colloidal stability and showed suitable properties for biomedical applications: being guided by an external magnetic field gradient created by a small permanent magnet, they also showed an important contrast enhancement in Magnetic Resonance Imaging with a particularly low (subnanomolar) detection limit. Dual encapsulation of magnetic nanoparticles with doxorubicin in the biodegradable vesicular matrix is very promising as a versatile method to prepare multifunctional drug nanocarriers. The drug release rate could indeed be enhanced twice under the application of a RF oscillating magnetic field producing a local hyperthermia at the scale of the membranes.

The well-known hyperthermia effect of USPIOs was utilized here in a softer and gentler manner of action on the polymersomes' membrane permeability than by thermoablation, which is based on the melting temperature of a semicrystalline polycarbonate block. In future studies, we will enhance the RF-triggered release effect by using USPIOs with larger diameters (e. g., by a factor 2), which are known to exhibit much higher specific loss powers ( $\sim 100$  W/g or more). Apart from a higher thermal dissipation acting on the membrane fluidity and hence on the diffusion constants, those larger USPIOs will be partially ferrimagnetic, *i.e.* with a magnetic anisotropy energy  $E_a > k_B T$ . This might introduce another mechanism of membrane permeation, by direct rotation of the grains at the frequency of

the oscillating magnetic field. Such a mechanism would be reminiscent of the "molecular drill" effect<sup>123–125</sup> predicted long ago for lipid bilayers under mechanical stress by adsorption onto a corrugated surface.

To summarize, by exhibiting biocompatibility of the polymeric matrix, ease of preparation, contrast enhancement in MRI and triggered release under RF oscillating field, those hybrid vesicles are good candidates for the magneto-chemotherapeutic treatment of cancer. This work evidenced for the first time the concept of multifunctional polymersomes to combine imaging and therapy, opening new avenues to improve cancer treatments and to understand their mechanisms. The impact of such theranostic systems on tumor regression is currently under investigation.

## EXPERIMENTAL DETAILS

**Materials and Syntheses.** *Polymer, Drug and Buffers.* PTMC<sub>24</sub>-b-PGA<sub>19</sub> diblock copolymer was synthesized by ring-opening polymerization (ROP) of  $\gamma$ -Benzyl-L-glutamate *N*-carboxyanhydride initiated by an amino functionalized PTMC macroinitiator upon a previously published method.<sup>82</sup> All the experiments were conducted on a PTMC<sub>24</sub>-b-PGA<sub>19</sub> ( $M_n = 4900$  g/mol) block copolymer which presents a hydrophilic weight fraction of 50 wt % and a molar mass dispersity of 1.15. The solvent for nanoprecipitation (DMSO) was used without prior purification. Doxorubicin hydrochloride (CAS: 25316–40–9) was supplied by Discovery Fine Chemicals (Wimborne, UK). DOX was reconstituted in DMSO, stored at 5 °C and used within one month. Sodium chloride, Tris-HCl and Tris base were provided by Sigma.

*Iron Oxide Nanoparticles.* Superparamagnetic nanoparticles of maghemite ( $\gamma$ -Fe<sub>2</sub>O<sub>3</sub>), also called USPIOs, were synthesized by alkaline coprecipitation of iron(II) and iron(III) salts<sup>75</sup> and sorted according to their size by fractionated phase separations.<sup>76</sup> Briefly, the ionic strength was increased to screen the electrostatic interactions between the nanoparticles and obtain successive fractions of narrower size distribution, as measured all along the sorting process by vibrating sample magnetometry (VSM) and on the final sample by scattering techniques (SLS, DLS and SANS). For dispersion in CH<sub>2</sub>Cl<sub>2</sub>, the surface of the nanoparticles was grafted by the anionic surfactant Beycostat NB09 (CECA, Arkema group, France) used to disperse inorganic pigments in aromatic and chlorinated oils (but insoluble in aliphatic solvents), which is a mixture of mono- and diesters of phosphoric acid. The grafting procedure (30 min at 60 °C, 20 mol % relatively to iron) was previously described.<sup>77</sup>

**Preparation of Empty, USPIO Loaded and DOX/USPIO Dual-Loaded Vesicles.** Carbonate buffer (pH 10.5, 50 mM, 4.5 mL) was added onto PTMC<sub>24</sub>-b-PGA<sub>19</sub> (5 mg) dissolved in DMSO (0.5 mL) under magnetic stirring (1000 rpm) in a plastic tube (1.5 cm diameter), leading to a homogeneous dispersion of vesicles. A syringe pump controlled the water flow rate during injection. Two addition durations (5 s and 15 min respectively) of water solution into DMSO were used in order to tune the final average vesicle size. The resulting samples were respectively called WDi (for "instantaneous") and WD15. The organic solvent was then removed by extensive dialysis against 4 L Tris buffer replaced at least twice (10 mM Tris, pH 7.4, 25 °C ionic strength 150 mM).

USPIO loading was performed at different feed weight ratios (FWR) ( $\text{wt}_{\text{USPIO}}/\text{wt}_{\text{copolymer}}$ ) using the same nanoprecipitation method. A negligible volume of USPIO suspension in CH<sub>2</sub>Cl<sub>2</sub> (e. g.,  $V_{\text{CH}_2\text{Cl}_2}/V_{\text{water}} = 0.55\%$  for  $\text{wt}_{\text{USPIO}}/\text{wt}_{\text{polymer}} = 50\%$ ) was added into the DMSO/copolymer solution prior to the addition of water. For DOX/USPIO dual-loaded vesicles, doxorubicin hydrochloride was at first solubilized in the DMSO/copolymer solution at 2 mg/mL before mixing with the USPIOs. After water addition,

organic solvent and free DOX were removed by dialysis for 4 h with a membrane of 3500 g/mol MWCO against 4 L Tris buffer (10 mM Tris, pH 7.4; 30 °C, ionic strength 150 mM). The doxorubicin loading content (LC) was determined after vesicle rupture using sonication in a mixture containing 80% volume of DMSO. This solvent mixture induced the aggregation of USPIOs that were then separated by centrifugation (1 h, 10 000 rpm). Then the titration of DOX was performed from the UV absorbance at  $\lambda_{\text{max}} = 485$  nm using the known value for doxorubicin in a DMSO/Tris buffer (80/20 v/v) mixture as calibration (see Supporting Information S-5-g).

**Experimental Methods.** *Dynamic Light Scattering (DLS) and Static Light Scattering (SLS).* were performed using an ALV Laser goniometer, which consisted of a 35 mW HeNe linear polarized laser with a wavelength of 632.8 nm and an ALV-5000/EPP Multiple Tau Digital correlator with 125 ns initial sampling time. The samples were kept at constant temperature (25 °C) during all the experiments. The accessible scattering angle range ranged from 30° up to 150°. However, most of the dynamic measurements were carried out at 90°. Aliquots of the samples (1 mL in a 10 mm diameter cylindrical glass cell) were immersed in a filtered toluene bath. The data acquisition was done with the ALV-Correlator Control software and the counting time for DLS was fixed for each sample at 30 s. To perform light scattering in static mode, the differential refractive index increment  $dn/dc$  of PTMC<sub>24</sub>-b-PGA<sub>12</sub> vesicles in buffer was measured over a concentration range from 0.2 to 1 mg/mL by means of a differential refractometer (Wyatt Optilab rEX) operating at a wavelength of 658 nm and at 25 °C. A  $dn/dc$  value of  $0.3454 \pm 6 \times 10^{-4}$  mL/g was obtained for WDi vesicles loaded with 50 wt % USPIOs, which is larger than the value  $dn/dc = dn/d\Phi/d^{\text{USPIO}} = 1.08/5.1 = 0.21$  mL/g reported for pure USPIOs coated with the same Beycostat surfactant.<sup>126</sup> The mean hydrodynamic radii and polydispersity indexes (PDI) were determined using the second order cumulant analysis.

*Isotropic Small Angle Neutron Scattering (SANS) Measurements.* were performed on the PAXY spectrometer of the Laboratoire Léon Brillouin (CEA-Saclay, France) equipped with a two dimension detector made of 128 × 128 cells. We used two configurations: the first one with a sample-to-detector distance of  $D = 6.7$  m and a neutron wavelength of  $\lambda = 10$  Å to cover a  $q$  range of  $2.5 \times 10^{-3} - 2.5 \times 10^{-2}$  Å<sup>-1</sup>; the second one with  $D = 2$  m and  $\lambda = 6$  Å to cover a  $q$  range of  $2 \times 10^{-2} - 0.2$  Å<sup>-1</sup>. Full angular averaging of the detector cells at constant  $q$  was realized for the scattering patterns with the PASINET software available at [www-llb.cea.fr](http://www-llb.cea.fr).

The samples were prepared by nanoprecipitation, centrifuged and redispersed in the desired mixture of hydrogenated and deuterated solvents at a final concentration of 10 mg/mL. Three solvents were used in order to match the scattering

length densities of the various components of the loaded magnetic polymersomes and to focus the contrast on selected features (see Supporting Information S-a). The magnetic scattering length density of the USPIOs estimated from the magnetization at saturation  $M_s$  and the volume of the nanoparticles was  $\rho_{\text{mag}}^{\text{USPIO}} \approx 10^{10} \text{ cm}^{-2}$ . One solvent was pure  $\text{H}_2\text{O}$ , which allowed observing mainly the nuclear scattering of USPIO but also in a reduced way the copolymer signal. Pure  $\text{D}_2\text{O}$  almost matched the nuclear signal of the USPIOs: this scattering intensity revealed the fluctuation of the polymeric membrane together with the magnetic scattering of the USPIOs. Finally, the use of a  $\text{H}_2\text{O}/\text{D}_2\text{O}$  (65.6/34.4 v/v) mixture matching the copolymer scattering length density enabled to focus on the nuclear scattering of the USPIOs only. The calculated contrast of neutrons scattering-length densities between  $\gamma\text{-Fe}_2\text{O}_3$  and this  $\text{H}_2\text{O}/\text{D}_2\text{O}$  mixture was  $\Delta\rho = 5 \times 10^{10} \text{ cm}^{-2}$ . SANS measurements were done in 5 mm thick quartz cuvettes for  $\text{D}_2\text{O}$  or 1 mm thick ones for  $\text{H}_2\text{O}$  and  $\text{H}_2\text{O}/\text{D}_2\text{O}$  solvents to minimize the incoherent scattering. All the scattered intensity curves were corrected from the incoherent background of their proper solvents. They have been also normalized by the incoherent signal delivered by a 1 mm gap water sample in order to account for the efficiency of the detector cells. Absolute values of the scattering intensity,  $I(q)$  in  $\text{cm}^{-1}$ , were obtained from the direct determination of the number of neutrons in the incident beam and the detector cell solid angle.<sup>127,128</sup>

Here we mainly discuss the SANS signal obtained with USPIO loaded polymersomes' suspensions in the  $\text{H}_2\text{O}/\text{D}_2\text{O}$  mixture, which matches the copolymer. Following a method used for other kinds of nanocomposites made from colloids or micelles,<sup>86,87</sup> the SANS curves of the USPIO loaded vesicles were divided by the volume fraction  $\Phi_{\text{USPIO}}$  and by the form factor of the USPIO nanoparticles measured independently on a dilute solution. This procedure yields the intra-aggregate structure factors  $S_{\text{intra}}(q)$  of the USPIO nanoparticles, which tell us about their spatial arrangement into aggregates of a given geometry (micellar, vesicular, fractal...). The calculated form factor of hollow shells took into account their radius, membrane thickness, dispersity and the experimental resolution of the spectrometer.<sup>88</sup>

**Anisotropic SANS Measurements.** The sample was placed between the poles of an electromagnet producing a homogeneous magnetic field at the sample position, as checked by a Hall probe (Walker scientific). The solvent used was pure  $\text{H}_2\text{O}$  which does not match the nuclear scattering length density of the copolymer but is ensuring a negligible magnetic scattering of iron oxide ( $\Delta\rho = 1.4 \times 10^{10} \text{ cm}^{-2}$  between  $\text{H}_2\text{O}$  and the magnetic scattering length density of iron oxide). Nevertheless, the nuclear contrast of the USPIO ( $\Delta\rho = 7.5 \times 10^{10} \text{ cm}^{-2}$ ) remained still three times larger than the one of the copolymer ( $\Delta\rho = 2.5 \times 10^{10} \text{ cm}^{-2}$ ). The scattering intensity being proportional to the square of the contrast, we can neglect the contribution arising both from the copolymer and from the magnetic moments of the USPIOs in the total scattered intensity. An anisotropic analysis was applied to the scattering patterns obtained under magnetic field. To obtain anisotropic curves with a good statistics, the intensity on the 2D-detector was averaged in angular sectors either  $[-30^\circ; 30^\circ]$  along the field direction where the scattered intensity was weaker, and thus called  $I^{\parallel}(q)$ , or  $[-15^\circ; 15^\circ]$  around the perpendicular direction and denoted  $I^{\perp}(q)$ .

**Magnetization Measurements.** The magnetization curves of the maghemite USPIOs and of the USPIO-loaded vesicles were determined using a homemade vibrating sample magnetometer (VSM) under an applied magnetic field up to 0.93 T. From the shape of the magnetization versus field intensity curve  $M(H)$ , the size distribution of the magnetic cores was obtained by convolving the first order Langevin's law of paramagnetism  $L_1(\xi) = M/\Phi m_s = \coth(\xi) - 1/\xi$  with  $\xi = \mu_0 m_s \pi D^3 H / 6 k_B T$  ( $k_B$  is the Boltzmann constant and  $\mu_0$  the vacuum magnetic permeability) with a Log-normal probability law of median diameter  $D_{\text{mag}}^{\text{USPIO}}$  and width  $\sigma$ , defined as the standard deviation of the distribution  $\text{Ln}(D/D_{\text{mag}}^{\text{USPIO}})$ .<sup>80,81</sup>

**Magnetic Birefringence.** The setup that has been described precisely<sup>129</sup> was improved for temperature control. Briefly, it

consisted in an electromagnet used to magnetically induce a macroscopic birefringence in a magnetic colloid made of birefringent magnetic nanoparticles (or made of nano-objects filled with such MNPs). This induced birefringence was then measured by sending a linearly polarized He/Ne laser beam (10 mW) through the birefringent sample and analyzing the transmitted light with a second polarizer and a photodiode. A photoelastic modulator and a lock-in amplifier were used to increase the setup sensitivity, the resulting AC and DC signals being related respectively to the levels of birefringence and dichroism under the applied magnetic field. To perform measurements at various controlled temperatures, the glass cell containing the sample was put in a specifically designed copper cell, which temperature was regulated using a Pt100 temperature probe and Peltier devices connected to a current source and externally controlled by a PC using NI LabVIEW.

**Magnetophoresis.** A magnetophoretic experiment consists in measuring the constant velocity reached by magnetic objects in a magnetic field of increasing intensity (spatial gradient), applying on them a magnetic force balanced by a viscous drag one.<sup>62,92,93,95,97,104</sup> In our case, a drop of an aqueous vesicle solution was placed between a glass slide, a 200  $\mu\text{m}$  spacer and a coverslip to prevent evaporation and convection. This cell was mounted on the stage of an inverted optical microscope (Leica DM-IL). A strong NdFeB magnet of 22 mm diameter and 10 mm thickness (Aimants Calamit, France) was held by a clip 6 mm away from the center of the focus plane of the microscope. Bright field optical microscopy images taken with a 40X objective were recorded with a digital camera (Infinity3-1U, Lumenera, Ottawa, Ontario, Canada) enabling pixel-binning to enhance the recording rate. The magnetophoretic trajectories of about 280 vesicles exhibiting a biased thermal motion toward the magnet were recorded at video rate (24 frames/s). Three sequences (each containing 240 frames of  $800 \times 600$  pixels) were analyzed off-line using the "ParticleTracker" plug-in developed by the MOSAIC group at ETH Zürich for the free image processing software ImageJ with the following parameters: Kernel radius = 6, Cutoff radius = 0.0, Percentile = 0.6, Displacement = 5.0, Linkrange = 120.<sup>130</sup> Each stack of 240 frames (10 s duration) necessitated a computing time of 16 min with a 64-bit desktop PC with 4Gb RAM. For theoretical calculations of the number of USPIOs per vesicle from the average drift velocity, a magnetic field gradient  $\text{dB}/\text{dz} = 18.5 \text{ mT}/\text{mm}$  and an average magnetic flux density  $B_0 = \mu_0 H_0 = 174 \text{ mT}$  were used as reported for an identical magnet.<sup>93</sup>

**MRI Relaxometry.** For different USPIO-vesicle formulations,  $T_1$  and  $T_2$  relaxivities were measured at 4.7 T ( $f_{\text{Larmor}} = 200 \text{ MHz}$ ) on a research MRI system (Bruker Biospec 47/50, Ettlingen, Germany) at 20 °C. The transverse  $T_2$  measurements were acquired using a multiple spin-echo 2D imaging sequence ( $T_R = 10\,000 \text{ ms}$ ; inter echo-time, 5 ms; number of echo images, 256; FOV,  $50 \times 50 \text{ mm}$ ; matrix,  $128 \times 128$ ; slice thickness, 1 mm). The longitudinal relaxation times  $T_1$  were obtained out using an inversion-recovery 2D imaging sequence (increment of inversion delay: 34 ms with 456 increments) followed by a RARE imaging sequence (RARE Factor: 8;  $T_R/T_E^{\text{eff}}$ : 10 000/7.7 ms; FOV:  $50 \times 50 \text{ mm}$ ; matrix:  $128 \times 128$ ; slice thickness: 1 mm). The relaxivity values  $r_1$  and  $r_2$  were calculated by linear fits of the relaxation rates  $1/T_1$  and  $1/T_2$  ( $\text{s}^{-1}$ ) vs iron concentration (mM) or vesicle concentration (nM).

**Iron Titration.** The total iron concentration (mol/L) was determined by atomic absorption spectroscopy (AAS) with a Perkin-Elmer Analyst 100 apparatus after degrading the USPIO-loaded vesicles in boiling HCl (35%). The volume fraction of iron oxide was deduced from the molar mass (159.7 g/mol) and mass density ( $5.1 \text{ g}/\text{cm}^3$ ) of  $\gamma\text{-Fe}_2\text{O}_3$ , that is, numerically  $\Phi_{\text{USPIO}} (\% \text{ v/v}) = 1.577 [\text{Fe}] (\text{mol}/\text{L})$ .

**Electrophoretic Mobility.** Empty and loaded vesicles were analyzed with a ZetaSizer NanoZS (Malvern Instruments, Worcestershire, UK). The electrophoretic mobility ( $\mu$ ) was converted into zeta potential ( $\zeta$ ) using Smoluchowski's approximation, which is valid since the vesicles are all much larger than the Debye length  $\kappa_D^{-1}$  of the buffers ( $\kappa_D D_H \gg 1$ ). All the measurements were performed at 25 °C and the data were at least the average of triplicate values.

**Transmission Electron Microscopy.** TEM images were recorded on a Hitachi H7650 microscope working at 80 kV equipped with a GATAN Orius 11 Megapixel camera. Samples were prepared by spraying a 1 mg/mL solution of the vesicles onto a copper grid coated with carbon (200 mesh) using a homemade spray tool.

**TEM with Negative Staining.** USPIO-loaded polymer vesicles (0.04 mg/mL in water) were adsorbed on a carbon-coated EM grid and negatively stained with 1% uranyl acetate. TEM was performed with a CM120 (FEI) microscope.

**Cryo-TEM Imaging.** USPIO-loaded polymer vesicles (2 mg/mL in water) were deposited on an EM grid coated with a perforated carbon film. After draining the excess liquid with a filter paper, grids were quickly plunged into liquid ethane and mounted onto a Gatan 626 cryoholder. TEM was performed with a Tecnai F20 (FEI) microscope operated at 200 kV. The images were recorded with a 5 Megapixel USC1000-SSCCD camera (Gatan).

**Atomic Force Microscopy.** AFM images were recorded in air with a Nanoscope IIIa microscope operating in dry Tapping-mode. The probes were commercially available silicon tips with a spring constant of 42 N/m, a resonance frequency of 285 kHz and a typical radius of curvature in the 10–12 nm range. Freshly cleaved mica was used as sample substrate materials. For the observation of empty and USPIO loaded vesicles, sample solutions in water at concentrations of 0.01 mg/mL and 0.1 mg/mL respectively were deposited on the substrate (20  $\mu$ L) and dried under vacuum at 40 °C for 12 h.

**In vitro DOX Release.** The required quantity of drug-loaded vesicles was poured into a dialysis tubing (Spectra/Por Float-A-Lyzer, 50 000 g/mol MWCO, 10 mm diameter, 10 mL volume). The dialysis membrane filled with 5 mL of DOX loaded polymersomes was introduced into a bath of 50 mL buffer (10 mM Tris, pH 7.4, ionic strength 150 mM). At each sampling point, sink conditions were maintained by replacing 2 mL of the outer medium reservoir by fresh buffer. Because of the known sensitivity of DOX to degradation, the amount of released drug was calculated by the difference between the initial drug content and the drug remaining at each sampling point in the suspension of vesicles. More precisely, a spectrophotometric measurement at  $\lambda_{\text{max}} = 485$  nm was performed on an aliquot taken inside the dialysis bag. To take into account absorption by iron oxide and turbidity, the DOX concentration was calculated from the measured absorbance using a calibration curve in water after subtracting the absorbance value of similar USPIO-loaded vesicles. Another method consisted in redispersing the vesicles inside the aliquots into individual components (USPIOs, molecular DOX and copolymer unimers) in a DMSO/Tris (80:20) mixture before measuring the absorbance. Their calibration curves being provided as Supporting Information S-g, both methods led to comparable results, attesting the reliability of the measurements.

**In vitro DOX Release under an Oscillating RF Magnetic Field.** We used a RF generator built at the ICMCB laboratory in Pessac, France.<sup>131,132</sup> An alternating magnetic field with  $f_{\text{RF}} = 500$  kHz frequency and mean field intensity  $H_0 = 2.12$  kA/m (induction  $B_0 = \mu_0 H_0 = 2.65$  mT) was generated by a 28-turn pancake coil (20 cm height) cooled by a water circulation. The frequency was adjusted by a Celes inductor C97104 (Celem Passive Components, Israel). The electrical current was provided by a wave generator (F11202, Française d'Instrumentation, France) connected to a power amplifier (AR Worldwide 800A3, 10kHz–3 MHz, EMV, France). The vesicles were prepared as usual then diluted by a factor 2. A dialysis bag filled with half of the dispersion (4 mL) was placed inside a plastic cylindrical vessel filled with 30 mL Tris buffer, fitting inside the coil of the above-described setup. The release profile of the other half was performed in the same conditions of volumes, vessels and ambient temperature of the room (23 °C), but kept far away from the magnetic field as a control experiment of release without RF field. In particular, both reservoirs of release medium were not stirred to avoid any parasitic heating due to the presence of a magnetic bar inside the RF magnetic field.

**Acknowledgment.** We thank E. Duguet, L. Raison, and S. Mornet for access to the magnetic hyperthermia setup at ICMCB (Pessac) and D. Talbot from PECSA laboratory (Paris) for titration by AAS. C.S. benefited from a PhD fellowship funded by CNRS and Conseil Régional d'Aquitaine. Financial support was provided by the European Commission through the Seventh Framework Program (FP7) for Research & Development (CP-IP 213631-2 NANOTHER).

**Supporting Information Available:** Contrasts and treatments of the SANS data of  $\gamma$ -Fe<sub>2</sub>O<sub>3</sub> USPIOs embedded within the membrane of poly(trimethylene carbonate)-*b*-poly(L-glutamic acid) (PTMC-*b*-PGA) vesicles. Shape anisotropy of the vesicles and variation of their membrane thickness under magnetic field. SANS study of magnetic vesicles in D<sub>2</sub>O. Magnetization of USPIO-loaded vesicles. Magnetic birefringence of USPIO-loaded vesicles. Calibration curves for DOX titration by spectrophotometry. Additional AFM images of bare and USPIO-loaded vesicles. Static light scattering (Zimm plot) of USPIO-loaded vesicles. Movies of the pure Brownian motion of vesicles (without magnetic field) and of their drift motion by magnetophoresis (under a field gradient). This material is available free of charge via the Internet at <http://pubs.acs.org>.

## REFERENCES AND NOTES

- Lee, C. C.; Gillies, E. R.; Fox, M. E.; Guillaudeu, S. J.; Fréchet, J. M. J.; Dy, E. E.; Szoka, F. C.; Single, A. Dose of Doxorubicin-Functionalized Bow-Tie Dendrimer Cures Mice Bearing C-26 Colon Carcinomas. *Proc. Natl. Acad. Sci. U.S.A.* **2006**, *103*, 16649–16654.
- Tong, R.; Christian, D. A.; Tang, L.; Cabral, H.; Baker, J.; James, R.; Kataoka, K.; Discher, D. E.; Cheng, J. Nanopolymeric Therapeutics. *MRS Bull.* **2009**, *34*.
- Singh, R.; Lillard, J. W., Jr Nanoparticle-Based Targeted Drug Delivery. *Exp. Mol. Pathol.* **2009**, *86*, 215–223.
- Upadhyay, K. K.; Agrawal, H. G.; Upadhyay, C.; Schatz, C.; Meins, J.-F. L.; Misra, A.; Lecommandoux, S. Role of Block Copolymer Nanoconstructs in Cancer Therapy. *Crit. Rev. Ther. Drug Carrier Syst.* **2009**, *26*, 157–205.
- Duncan, R. Polymer Conjugates as Anticancer Nanomedicines. *Nat. Rev. Cancer* **2006**, *6*, 688–701.
- Peer, D.; Karp, J. M.; Hong, S.; Farokhzad, O. C.; Margalit, R.; Langer, R. Nanocarriers as an Emerging Platform for Cancer Therapy. *Nat. Nano* **2007**, *2*, 751–760.
- Fox, M. E.; Guillaudeu, S.; Fréchet, J. M. J.; Jerger, K.; Macaraeg, N.; Szoka, F. C. Synthesis and *In Vivo* Antitumor Efficacy of PEGylated Poly(L-lysine) Dendrimer–Camptothecin Conjugates. *Mol. Pharmaceutics* **2009**, *6*, 1562–1572.
- Levine, D. H.; Ghoroghchian, P. P.; Freudenberg, J.; Zhang, G.; Therien, M. J.; Greene, M. I.; Hammer, D. A.; Murali, R.; Polymersomes, A. New Multi-Functional Tool for Cancer Diagnosis and Therapy. *Methods* **2008**, *46*, 25–32.
- Blanazs, A.; Armes, S. P.; Ryan, A. J. Self-Assembled Block Copolymer Aggregates: From Micelles to Vesicles and Their Biological Applications. *Macromol. Rapid Commun.* **2009**, *30*, 267–277.
- Christian, D. A.; Cai, S.; Bowen, D. M.; Kim, Y.; Pajeroski, J. D.; Discher, D. E. Polymersome Carriers: From Self-Assembly to siRNA and Protein Therapeutics. *Eur. J. Pharm. Biopharm.* **2009**, *71*, 463–474.
- Du, J.; O'Reilly, R. K. Advances and Challenges in Smart and Functional Polymer Vesicles. *Soft Matter* **2009**, *5*, 3544–3561.
- LoPresti, C.; Lomas, H.; Massignani, M.; Smart, T.; Battaglia, G. Polymersomes: Nature Inspired Nanometer Sized Compartments. *J. Mater. Chem.* **2009**, *19*, 3576–3590.
- Ahmed, F.; Pakunlu, R. I.; Brannan, A.; Bates, F.; Minko, T.; Discher, D. E. Biodegradable Polymersomes Loaded with Both Paclitaxel and Doxorubicin Permeate and Shrink Tumors, Inducing Apoptosis in Proportion to Accumulated Drug. *J. Controlled Release* **2006**, *116*, 150–158.

14. Ahmed, F.; Pakunlu, R. I.; Srinivas, G.; Brannan, A.; Bates, F.; Klein, M. L.; Minko, T.; Discher, D. E. Shrinkage of a Rapidly Growing Tumor by Drug-Loaded Polymer-somes: pH-Triggered Release Through Copolymer Degradation. *Mol. Pharmaceutics* **2006**, *3*, 340–350.
15. Li, M.-H.; Keller, P. Stimuli-Responsive Polymer Vesicles. *Soft Matter* **2009**, *5*, 927–937.
16. Meng, F.; Zhong, Z.; Feijen, J. Stimuli-Responsive Polymersomes for Programmed Drug Delivery. *Biomacromolecules* **2009**, *10*, 197–209.
17. Onaca, O.; Enea, R.; Hughes, D. W.; Meier, W. Stimuli-Responsive Polymersomes as Nanocarriers for Drug and Gene Delivery. *Macromol. Biosci.* **2009**, *9*, 129–139.
18. Ahmed, F.; Discher, D. E. Self-Porting polymersomes of PEG-PLA and PEG-PCL: Hydrolysis-Triggered Controlled Release Vesicles. *J. Controlled Release* **2004**, *96*, 37–53.
19. Meng, F.; Engbers, G. H. M.; Feijen, J. Biodegradable Polymersomes as a Basis for Artificial Cells: Encapsulation, Release and Targeting. *J. Controlled Release* **2005**, *101*, 187–198.
20. Lu, Z.-R.; Ye, F.; Vaidya, A. Polymer Platforms for Drug Delivery and Biomedical Imaging. *J. Controlled Release* **2007**, *122*, 269–277.
21. Kyeongsoon, P.; Seulki, L.; Eunah, K.; Kwangmeyung, K.; Kuiwon, C.; Ick Chan, K. New Generation of Multifunctional Nanoparticles for Cancer Imaging and Therapy. *Adv. Funct. Mat.* **2009**, *19*, 1553–1566.
22. Boppart, S. A.; Oldenburg, A. L.; Xu, C.; Marks, D. L. Optical Probes and Techniques for Molecular Contrast Enhancement in Coherence Imaging. *J. Biomed. Opt.* **2005**, *10*, 041208–14.
23. Sancey, L.; Dufort, S.; Jossierand, V.; Keramidias, M.; Righini, C.; Rome, C.; Faure, A. C.; Foillard, S.; Roux, S.; Boturyn, D.; et al. Drug Development in Oncology Assisted by Noninvasive Optical Imaging. *Int. J. Pharm.* **2009**, *379*, 309–316.
24. Ghoroghchian, P. P.; Frail, P. R.; Susumu, K.; Blessington, D.; Brannan, A. K.; Bates, F. S.; Chance, B.; Hammer, D. A.; Therien, M. J. Near-Infrared-Emissive Polymer-somes: Self-Assembled Soft Matter for *In Vivo* Optical Imaging. *Proc. Natl. Acad. Sci. U.S.A.* **2005**, *102*, 2922–2927.
25. Berridge, M. S.; Heald, D. L.; Lee, Z. Imaging Studies of Biodistribution and Kinetics in Drug Development. *Drug Dev. Res.* **2003**, *59*, 208–226.
26. Meikle, S. R.; Kench, P.; Kassiou, M.; Banati, R. B. Small Animal SPECT and its Place in the Matrix of Molecular Imaging Technologies. *Phys. Med. Biol.* **2005**, *50*, R45–R61.
27. Gillies, E. R.; Dy, E.; Fréchet, J. M. J.; Szoka, F. C. Biological Evaluation of Polyester Dendrimer: Poly(ethylene oxide)“Bow-Tie” Hybrids with Tunable Molecular Weight and Architecture. *Mol. Pharmaceutics* **2005**, *2*, 129–138.
28. Seydel, C. Quantum Dots Get Wet. *Science* **2003**, *300*, 80–81.
29. Gao, X.; Cui, Y.; Levenson, R. M.; Chung, L. W. K.; Nie, S. *In Vivo* Cancer Targeting and Imaging with Semiconductor Quantum Dots. *Nat. Biotechnol.* **2004**, *22*, 969–976.
30. So, M.-K.; Xu, C.; Loening, A. M.; Gambhir, S. S.; Rao, J. Self-Illuminating Quantum Dot Conjugates for *In Vivo* Imaging. *Nat. Biotechnol.* **2006**, *24*, 339–343.
31. Loo, C.; Lin, A.; Hirsch, L.; Lee, M.-H.; Barton, J.; Halas, N.; West, J.; Dresek, R. Nanoshell-Enabled Photonics-Based Imaging and Therapy of Cancer. *Techn. Cancer Res. Treat.* **2004**, *3*, 33–39.
32. Hainfeld, J. F.; Slatkin, D. N.; Smilowitz, H. M. The Use of Gold Nanoparticles to Enhance Radiotherapy in Mice. *Phys. Med. Biol.* **2004**, *49*, N309–N315.
33. Huang, X.; El-Sayed, I. H.; Qian, W.; El-Sayed, M. A. Cancer Cell Imaging and Photothermal Therapy in the Near-Infrared Region by Using Gold Nanorods. *J. Am. Chem. Soc.* **2006**, *128*, 2115–2120.
34. Park, H.; Yang, J.; Lee, J.; Haam, S.; Choi, I.-H.; Yoo, K.-H. Multifunctional Nanoparticles for Combined Doxorubicin and Photothermal Treatments. *ACS Nano* **2009**, *3*, 2919–2926.
35. Hu, K.-W.; Liu, T.-M.; Chung, K.-Y.; Huang, K.-S.; Hsieh, C.-T.; Sun, C.-K.; Yeh, C.-S. Efficient Near-IR Hyperthermia and Intense Nonlinear Optical Imaging Contrast on the Gold Nanorod-in-Shell Nanostructures. *J. Am. Chem. Soc.* **2009**, *131*, 14186–14187.
36. Khemtong, C.; Kessinger, C. W.; Gao, J. Polymeric Nanomedicine for Cancer MR Imaging and Drug Delivery. *Chem. Commun.* **2009**, 3497–3510.
37. Liu, T.-Y.; Hu, S.-H.; Liu, D.-M.; Chen, S.-Y.; Chen, I. W. Biomedical Nanoparticle Carriers with Combined Thermal and Magnetic Responses. *Nano Today* **2009**, *4*, 52–65.
38. These USPIO nanocrystals present no magnetization in the absence of magnetic field due to thermal agitation but their assembly, also called “ferrofluid”, exhibits a strong magnetic susceptibility under a field of low intensity, thus combining the property of superparamagnetism with the advantage of being a stable colloidal suspension.
39. Mornet, S.; Vasseur, S.; Gasset, F.; Duguet, E. Magnetic Nanoparticle Design for Medical Diagnosis and Therapy. *J. Mater. Chem.* **2004**, *14*, 2161–2175.
40. Neuberger, T.; Schopf, B.; Hofmann, H.; Hofmann, M.; von Rechenberg, B. Superparamagnetic Nanoparticles for Biomedical Applications: Possibilities and Limitations of a New Drug Delivery System. *J. Magn. Magn. Mater.* **2005**, *293*, 483–496.
41. Laurent, S.; Forge, D.; Port, M.; Roch, A.; Robic, C.; Vander Elst, L.; Muller, R. N. Magnetic Iron Oxide Nanoparticles: Synthesis, Stabilization, Vectorization, Physicochemical Characterizations, and Biological Applications. *Chem. Rev.* **2008**, *108*, 2064–2110.
42. Sun, C.; Lee, J. S. H.; Zhang, M. Magnetic Nanoparticles in MR Imaging and Drug Delivery. *Adv. Drug Delivery Rev.* **2008**, *60*, 1252–1265.
43. Veisheh, O.; Gunn, J. W.; Zhang, M. Design and Fabrication of Magnetic Nanoparticles for Targeted Drug Delivery and Imaging. *Adv. Drug Delivery Rev.* **2010**, *62*, 284–304.
44. Shubayev, V. I.; Pisanic, I. T. R.; Jin, S. Magnetic Nanoparticles for Theragnostics. *Adv. Drug Delivery Rev.* **2009**, *61*, 467–477.
45. Gossuin, Y.; Gillis, P.; Hocq, A.; Vuong, Q. L.; Roch, A. Magnetic Resonance Relaxation Properties of Superparamagnetic Particles. *Wiley Interdiscip. Rev.: Nanomed. Nanobiotechnol.* **2008**, *1*, 299–310.
46. Rabin, Y. Is Intracellular Hyperthermia Superior to Extracellular Hyperthermia in the Thermal Sense? *Int. J. Hyperthermia* **2002**, *18*, 194–202.
47. Thiesen, B.; Jordan, A. Clinical Applications of Magnetic Nanoparticles for Hyperthermia. *Int. J. Hyperthermia* **2008**, *24*, 467–474.
48. Bellizzi, G.; Bucci, O. On the Optimal Choice of the Exposure Conditions and the Nanoparticle Features in Magnetic Nanoparticle Hyperthermia. *Int. J. Hyperthermia* **2010**, *26*, 389–403.
49. Hergt, R.; Andra, W.; d’Ambly, C. G.; Hilger, I.; Kaiser, W. A.; Richter, U.; Schmidt, H. G. Physical Limits of Hyperthermia Using Magnetite Fine Particles. *IEEE Trans. Magn.* **1998**, *34*, 3745–3754.
50. Rosensweig, R. E. Heating Magnetic Fluid with Alternating Magnetic Field. *J. Magn. Magn. Mater.* **2002**, *252*, 370–374.
51. Chastellain, M.; Petri, A.; Gupta, A.; Rao, K. V.; Hofmann, H. Superparamagnetic Silica-Iron Oxide Nanocomposites for Application in Hyperthermia. *Adv. Eng. Mater.* **2004**, *6*, 235–241.
52. Hergt, R.; Zeisberger, R. H.; Schüler, D.; Heyen, U.; Hilger, I.; Kaiser, W. A. Magnetic Properties of Bacterial Magnetosomes as Potential Diagnostic and Therapeutic Tools. *J. Magn. Magn. Mater.* **2005**, *293*, 80–86.



53. Glöckl, G.; Hergt, R.; Zeisberger, M.; Dutz, S.; Nagel, S.; Weitschies, W. The Effect of Field Parameters, Nanoparticle Properties and Immobilization on the Specific Heating Power in Magnetic Particle Hyperthermia. *J. Phys.: Condens. Matter* **2006**, *18*, S2935–S2949.
54. Fortin, J.-P.; Wilhelm, C.; Servais, J.; Ménager, C.; Bacri, J.-C.; Gazeau, F. Size-Sorted Anionic Iron Oxide Nanomagnets as Colloidal Mediators for Magnetic Hyperthermia. *J. Am. Chem. Soc.* **2007**, *129*, 2628–2635.
55. Jordan, A. Inductive Heating of Ferrimagnetic Particles and Magnetic Fluids: Physical Evaluation of Their Potential for Hyperthermia. *Int. J. Hyperthermia* **2009**, *25*, 512–516.
56. Ahrentorp, F.; Astalan, A.; Jonasson, C.; Blomgren, J.; Bin, Q.; Thompson Meford, O.; Yan, M.; Courtois, J.; Berret, J.-F.; Fresnais, J. *et al.* Sensitive High Frequency AC Susceptometry in Magnetic Nanoparticle Applications. In *The 8th International Conference on the Scientific and Clinical Applications of Magnetic Carriers*; Häfeli, U., Schütt, W., Zborowski, M., Eds.; AIP Conference Proceedings Series: Rostock, Germany, 2010; Vol. 1311, pp 213–223.
57. Aquil, A.; Vasseur, S.; Duguet, E.; Passirani, C.; Benoît, J.-P.; Roch, A.; Muller, R. N.; Jérôme, R.; Jérôme, C. PEO Coated Magnetic Nanoparticles for Biomedical Application. *Eur. Polym. J.* **2008**, *44*, 3191–3199.
58. Bulte, J. W. M.; De Cuyper, M.; Despres, D.; Frank, J. A. Preparation, Relaxometry, and Biokinetics of PEGylated Magnetoliposomes as MR Contrast Agent. *J. Magn. Magn. Mater.* **1999**, *194*, 204–209.
59. Bulte, J. W. M.; De Cuyper, M.; Nejat, D., Magnetoliposomes as Contrast Agents. In *Methods in Enzymology*; Academic Press: New York, 2003; Vol. 373, pp 175–198.
60. Bacri, J.-C.; Cabuil, V.; Cebers, A.; Ménager, C.; Perzynski, R. Flattening of Ferro-Vesicle Undulations Under a Magnetic Field. *Europhys. Lett.* **1996**, *33*, 235–240.
61. Sandre, O.; Ménager, C.; Prost, J.; Cabuil, V.; Bacri, J.-C.; Cebers, A. Shape Transitions of Giant Liposomes Induced by an Anisotropic Spontaneous Curvature. *Phys. Rev. E* **2000**, *62*, 3865–3870.
62. Beaune, G.; Ménager, C.; Cabuil, V. Location of Magnetic and Fluorescent Nanoparticles Encapsulated inside Giant Liposomes. *J. Phys. Chem. B.* **2008**, *112*, 7424–7429.
63. Babincová, M.; Cicmanec, P.; Altanerová, V.; Altaner, C.; Babinec, P. AC-Magnetic Field Controlled Drug Release From Magnetoliposomes: Design of a Method for Site-Specific Chemotherapy. *Bioelectrochemistry* **2002**, *55*, 17–19.
64. Pradhan, P.; Giri, J.; Rieken, F.; Koch, C.; Mykhaylyk, O.; Döblinger, M.; Banerjee, R.; Bahadur, D.; Plank, C. Targeted Temperature Sensitive Magnetic Liposomes for Thermo-Chemotherapy. *J. Controlled Release* **2010**, *142*, 108–121.
65. Xiang, T.-X.; Anderson, B. D. Phase Structures of Binary Lipid Bilayers as Revealed by Permeability of Small Molecules. *Biochim. Biophys. Acta, Biomembr.* **1998**, *1370*, 64–76.
66. Chen, Y.; Bose, A.; Bothun, G. D. Controlled Release from Bilayer-Decorated Magnetoliposomes via Electromagnetic Heating. *ACS Nano* **2010**, *4*, 3215–3222.
67. Kuznetsov, A. A.; Filippov, V. I.; Alyautdin, R. N.; Torshina, N. L.; Kuznetsov, O. A. Application of Magnetic Liposomes for Magnetically Guided Transport of Muscle Relaxants and Anti-Cancer Photodynamic Drugs. *J. Magn. Magn. Mater.* **2001**, *225*, 95–100.
68. Fortin-Ripoche, J.-P.; Martina, M. S.; Gazeau, F.; Ménager, C.; Wilhelm, C.; Bacri, J.-C.; Lesieur, S.; Clément, O. Magnetic Targeting of Magnetoliposomes to Solid Tumors with MR Imaging Monitoring in Mice: Feasibility. *Radiology* **2006**, *239*, 415–424.
69. Wijaya, A.; Hamad-Schifferli, K. High-Density Encapsulation of Fe<sub>3</sub>O<sub>4</sub> Nanoparticles in Lipid Vesicles. *Langmuir* **2007**, *23*, 9546–9550.
70. Discher, D. E.; Eisenberg, A. Polymer Vesicles. *Science* **2002**, *297*, 967–973.
71. Lecommandoux, S.; Sandre, O.; Chécot, F.; Rodriguez-Hernandez, J.; Perzynski, R. Magnetic Nanocomposite Micelles and Vesicles. *Adv. Mater.* **2005**, *17*, 712–718.
72. Lecommandoux, S.; Sandre, O.; Chécot, F.; Rodriguez-Hernandez, J.; Perzynski, R. Self-Assemblies of Magnetic Nanoparticles and Di-block Copolymers: Magnetic Micelles and Vesicles. *J. Magn. Magn. Mater.* **2006**, *300*, 71–74.
73. Lecommandoux, S.; Sandre, O.; Chécot, F.; Perzynski, R. Smart Hybrid Magnetic Self-Assembled Micelles and Hollow Capsules. *Prog. Solid State Chem.* **2006**, *34*, 171–179.
74. Krack, M.; Hohenberg, H.; Kornowski, A.; Lindner, P.; Weller, H.; Förster, S. Nanoparticle-Loaded Magnetophoretic Vesicles. *J. Am. Chem. Soc.* **2008**, *130*, 7315–7320.
75. Massart, R. Preparation of Aqueous Magnetic Liquid in Alkaline and Acidic Media. *IEEE Trans. Magn.* **1981**, *17*, 1247.
76. Massart, R.; Dubois, E.; Cabuil, V.; Hasmonay, E. Preparation and Properties of Monodisperse Magnetic Fluids. *J. Magn. Magn. Mater.* **1995**, *149*, 1–5.
77. Da Cruz, C.; Sandre, O.; Cabuil, V. Phase Behavior of Nanoparticles in a Thermotropic Liquid Crystal. *J. Phys. Chem. B* **2005**, *109*, 14292–14299.
78. Kunz, D.; Thurn, A.; Burchard, W. Dynamic Light Scattering from Spherical Particles. *Colloid Polym. Sci.* **1983**, *261*, 635–644.
79. Burchard, W., Static and Dynamic Light Scattering from Branched Polymers and Biopolymers. In *Light Scattering from Polymers*; Springer: Heidelberg, 1983; Vol. 48, pp 1–124.
80. Chantrell, R. W.; Popplewell, J.; Charles, S. W. Measurements of Particle Size Distribution Parameters in Ferrofluids. *IEEE Trans. Magn.* **1978**, *MAG-14*, 975–977.
81. Bacri, J.-C.; Perzynski, R.; Salin, D.; Cabuil, V.; Massart, R. Phase Diagram of an Ionic Magnetic Colloid: Experimental Study of the Effect of Ionic Strength. *J. Colloid Interface Sci.* **1989**, *132*, 43–53.
82. Sanson, C.; Schatz, C.; Le Meins, J. F.; Brület, A.; Soum, A.; Lecommandoux, S. Biocompatible and Biodegradable Poly(trimethylene carbonate)-block-poly(L-glutamic acid) Polymersomes: Size Control and Stability. *Langmuir* **2010**, *26*, 2751–2760.
83. Sanson, C.; Le Meins, J. F.; Schatz, C.; Soum, A.; Lecommandoux, S. Temperature Responsive Poly(trimethylene carbonate)-block-poly(L-glutamic acid) Copolymer: Polymersomes Fusion and Fission. *Soft Matter* **2010**, *6*, 1722–1730.
84. Hickey, R. J.; Sanchez-Gaytan, B. L.; Cui, W.; Composto, R. J.; Fryd, M.; Wayland, B. B.; Park, S. J. Morphological Transitions of Block-Copolymer Bilayers via Nanoparticle Clustering. *Small* **2009**, *6*, 48–51.
85. Berry, G. C. Thermodynamic and Conformational Properties of Polystyrene. I. Light-Scattering Studies on Dilute Solutions of Linear Polystyrenes. *J. Chem. Phys.* **1966**, *44*, 4550–4564.
86. Oberdisse, J.; Couve, C.; Appell, J.; Berret, J.-F.; Ligoure, C.; Porte, G. Vesicles and Onions from Charged Surfactant Bilayers: A Neutron Scattering Study. *Langmuir* **1996**, *12*, 1212–1218.
87. Oberdisse, J.; Demé, B. Structure of Latex-Silica Nanocomposite Films: A Small-Angle Neutron Scattering Study. *Macromolecules* **2002**, *35*, 4397–4405.
88. Chécot, F.; Brület, A.; Oberdisse, J.; Gnanou, Y.; Mondain-Monval, O.; Lecommandoux, S. Structure of Polypeptide-Based Diblock Copolymers in Solution: Stimuli-Responsive Vesicles and Micelles. *Langmuir* **2005**, *21*, 4308–4315.
89. Bar, G.; Thomman, Y.; Brandsch, R.; Cantow, H. J.; Whangbo, M. H. Factors Affecting the Height and Phase Images in Tapping Mode Atomic Force Microscopy. Study of Phase-Separated Polymer Blends of Poly(ethylene-co-styrene) and Poly(2,6-dimethyl-1,4-phenylene oxide). *Langmuir* **1997**, *13*, 3807–3812.

90. Magonov, S. N.; Elings, V.; Whangbo, M. H. Phase Imaging and Stiffness in Tapping-Mode Atomic Force Microscopy. *Surface Sci. Lett.* **1997**, *375*, L385–L391.
91. The release of unbound USPIOs in water was indeed very unlikely because of their strong hydrophobic surface covered by the Beycostat surfactant. Taken several days after the preparation of the vesicles, the TEM images never exhibited individual nanoparticles or clusters that did not look as the hollow structures depicted in Figure 2. After attracting all the vesicles toward a strong magnet like during a magnetophoresis experiment, the solvent became colorless. Even with a sensitive analytical technique such as AAS, no traces of magnetic nanoparticles could be detected outside the membranes. This absence of detectable iron in the supernatant (*i.e.*, at a concentration below  $10^{-5}$  mol/L) combined with the VSM results strongly supports the fact that, concerning the USPIOs, the FWR (in the solvent mixture) and the LC (after nanoprecipitation and dialysis) are equal.
92. Letellier, D.; Ménager, C.; Cabuil, V.; Sandre, O.; Lavergne, M. Magnetic Tubules. *Mater. Sci. Eng., C* **1997**, *5*, 153–162.
93. Wilhelm, C.; Gazeau, F.; Bacri, J.-C. Magnetophoresis and Ferromagnetic Resonance of Magnetically Labeled Cells. *Eur. Biophys. J.* **2002**, *31*, 118–125.
94. Watarai, H.; Namba, M. Capillary Magnetophoresis of Human Blood Cells and Their Magnetophoretic Trapping in a Flow System. *J. Chromatogr., A* **2002**, *961*, 3–8.
95. Pamme, N.; Manz, A. On-Chip Free-Flow Magnetophoresis: Continuous Flow Separation of Magnetic Particles and Agglomerates. *Anal. Chem.* **2004**, *76*, 7250–7256.
96. Berret, J.-F.; Sandre, O.; Mauger, A. Size Distribution of Superparamagnetic Particles Determined by Magnetic Sedimentation. *Langmuir* **2007**, *23*, 2993–2999.
97. Cuevas, G. D. L.; Faraudo, J.; Camacho, J. Low-Gradient Magnetophoresis through Field-Induced Reversible Aggregation. *J. Phys. Chem. C* **2008**, *112*, 945–950.
98. Williams, P. S.; Carpino, F.; Zborowski, M. Magnetic Nanoparticle Drug Carriers and Their Study by Quadrupole Magnetic Field-Flow Fractionation. *Mol. Pharmaceutics* **2009**, *6*, 1290–1306.
99. Yu, F.; Zhang, L.; Huang, Y.; Sun, K.; David, A. E.; Yang, V. C. The Magnetophoretic Mobility and Superparamagnetism of Core-Shell Iron Oxide Nanoparticles with Dual Targeting and Imaging Functionality. *Biomaterials* **2010**, *31*, 5842–5848.
100. Loudet, J.-C.; Hanusse, P.; Poulin, P. Stokes Drag on a Sphere in a Nematic Liquid Crystal. *Science* **2004**, *306*, 1525. In our case, the histograms of elementary motions were built in both directions of the  $(x,y)$  plane of focus (Figure 5) for a total number of 64 519 steps at a time delay  $\tau = 1/24$  s and 3920 steps at  $2\tau$ . Those curves were fitted with Gaussian laws centered respectively around  $V_{x/y} \times \tau$  and  $V_{x/y} \times 2\tau$  with standard deviations  $\sigma_{x/y}(\tau) = (2D_{\text{ves}}\tau)^{1/2}$  and  $\sigma_{x/y}(2\tau) = (4D_{\text{ves}}\tau)^{1/2}$ .
101. The magnetic moment of the vesicle  $m$  is directly related to  $\mu^{\text{USPIO}}$ , the average magnetic moment of each of the encapsulated USPIO particles and to their degree of orientation under a mean field intensity value  $B_0$  given by Langevin's first order function  $L_1(\xi)$  with  $\xi = \mu^{\text{USPIO}}B_0/k_B T$  according to  $m = N^{\text{USPIO}} \times \mu^{\text{USPIO}} \times L_1(\xi)$ , where  $N^{\text{USPIO}}$  is the number of USPIO per vesicle. The magnetic moment per nanoparticle  $\mu^{\text{USPIO}}$  is simply the product of the specific magnetization  $m_s$  by  $V_{\text{USPIO}}$ . For the mean magnetic field intensity  $B_0 = 174$  mT in this magnetophoretic experiment, the USPIO-loaded vesicle magnetization  $M$  corresponds to 55% of its saturation value  $M_s$  ( $L_1(\xi) = 0.55$ , as seen in Figure S-4, Supporting Information).
102. Ménager, C.; Guemghar, D.; Perzynski, R.; Lesieur, S.; Cabuil, V. Lipid Bilayer Elasticity Measurements in Giant Liposomes in Contact with a Solubilizing Surfactant. *Langmuir* **2008**, *24*, 4968–4974.
103. Masoud, H.; Alexeev, A. Modeling Magnetic Microcapsules that Crawl in Microchannels. *Soft Matter* **2010**, *6*, 794–799.
104. Martina, M.-S.; Wilhlem, C.; Lesieur, S. The Effect of Magnetic Targeting on the Uptake of Magnetic-Fluid-Loaded Liposomes by Human Prostatic Adenocarcinoma Cells. *Biomaterials* **2008**, *29*, 4137–4145.
105. Tresilwised, N.; Pithayanukul, P.; Mykhaylyk, O.; Holm, P. S.; Holzmüller, R.; Anton, M.; Thalhammer, S.; Adigüzel, D.; Döblinger, M.; Plank, C. Boosting Oncolytic Adenovirus Potency with Magnetic Nanoparticles and Magnetic Force. *Mol. Pharmaceutics* **2010**, *7*, 1069–1089.
106. Darton, N. J.; Hallmark, B.; Han, X.; Palit, S.; Slater, N. K. H.; Mackley, M. R. The In-Flow Capture of Superparamagnetic Nanoparticles for Targeting Therapeutics. *Nanomed.: Nanotechnol., Biol. Med.* **2008**, *4*, 19–29.
107. Ai, H.; Flask, C.; Weinberg, B.; Shuai, X. T.; Pagel, M. D.; Farrell, D.; Duerk, J.; Gao, J. Magnetite-Loaded Polymeric Micelles as Ultrasensitive Magnetic-Resonance Probes. *Adv. Mater.* **2005**, *17*, 1949–1952.
108. Roch, A.; Muller, R. N.; Gillis, P. Theory of Proton Relaxation Induced by Superparamagnetic Particles. *J. Chem. Phys.* **1999**, *110*, 5403–5411.
109. Brillet, P.-Y.; Gazeau, F.; Luciani, A.; Bessoud, B.; Cuénod, C.-A.; Siauve, N.; Pons, J.-N.; Poupon, J.; Clément, O. Evaluation of Tumoral Enhancement by Superparamagnetic Iron Oxide Particles: Comparative Studies with Ferumoxtran and Anionic Iron Oxide Nanoparticles. *Eur. Radiol.* **2005**, *15*, 1369–1377.
110. Weissleder, R.; Starck, D. D.; Engelstad, B. L.; Bacon, B. R.; Compton, C. C.; White, D. L.; Jacobs, P.; Lewis, J. Superparamagnetic Iron Oxide: Pharmacokinetics and Toxicity. *Am. J. Roentgenol.* **1989**, *152*, 167–173.
111. Corot, C.; Robert, P.; Idée, J.-M.; Port, M. Recent Advances in Iron Oxide Nanocrystal Technology for Medical Imaging. *Adv. Drug Delivery Rev.* **2006**, *58*, 1471–1504.
112. Nasongkla, N.; Bey, E.; Ren, J.; Ai, H.; Khemtong, C.; Guthi, J. S.; Chin, S.-F.; Sherry, A. D.; Boothman, D. A.; Gao, J. Multifunctional Polymeric Micelles as Cancer-Targeted, MRI-Ultrasensitive Drug Delivery Systems. *Nano Lett.* **2006**, *6*, 2427–2430.
113. Jain, T. K.; Richey, J.; Strand, M.; Leslie-Pelecky, D. L.; Flask, C. A.; Labhasetwar, V. Magnetic Nanoparticles with Dual Functional Properties: Drug Delivery and Magnetic Resonance Imaging. *Biomaterials* **2008**, *29*, 4012–4021.
114. Martina, M.-S.; Fortin, J.-P.; Ménager, C.; Clément, O.; Barratt, G.; Grabielle-Madellmont, C.; Gazeau, F.; Cabuil, V.; Lesieur, S. Generation of Superparamagnetic Liposomes Revealed as Highly Efficient MRI Contrast Agents for *In Vivo* Imaging. *J. Am. Chem. Soc.* **2005**, *127*, 10676–10685.
115. Berret, J.-F.; Schonbeck, N.; Gazeau, F.; Kharrat, D. E.; Sandre, O.; Vacher, A.; Airiau, M. Controlled Clustering of Superparamagnetic Nanoparticles Using Block Copolymers: Design of New Contrast Agents for Magnetic Resonance Imaging. *J. Am. Chem. Soc.* **2006**, *128*, 1755–1761. These USPIOs were synthesized exactly as here and had an identical median diameter  $D_{\text{mag}}^{\text{USPIO}} = 6.3 \pm 0.1$  nm and size width  $\sigma = 0.23 \pm 0.02$ . The relaxivity was measured at 0.47 T but the value can be safely extrapolated at 9.4 T according to the saturation of  $r_2$  as a function of the field well known for USPIOs.
116. Roch, A.; Gossuin, Y.; Muller, R. N.; Gillis, P. Superparamagnetic colloid suspensions: Water magnetic relaxation and clustering. *J. Magn. Magn. Mater.* **2005**, *293*, 532–539. For USPIOs of magnetic core diameter 6.4 nm very close to ours, these authors localized the plateau of  $r_2$  for clusters' radii ranging from 33 to 132.5 nm due to the exit of the domain of validity of the Outer Sphere Diffusion model, where  $r_2$  varies like the square of the number of USPIOs and the inverse of the cluster size, and the crossover to the Static Dephasing Regime characterized by a constant  $r_2$ . Therefore all the WDi samples which have hydrodynamic radii around 50 nm correspond to the onset of this SDR model, which might

- explain why  $r_2$  starts to increase, but with a slower variation than a parabolic law, and then reaches a plateau for the two most highly loaded samples.
117. Pinho, S. L. C.; Pereira, G. A.; Voisin, P.; Kassem, J.; Bouchaud, V.; Etienne, L.; Peters, J. A.; Carlos, L.; Mornet, S.; Geraldes, C. F. G. C.; Rocha, J.; Delville, M.-H. Fine Tuning of the Relaxometry of  $\gamma$ -Fe<sub>2</sub>O<sub>3</sub>@SiO<sub>2</sub> Nanoparticles by Tweaking the Silica Coating Thickness. *ACS Nano* **2010**, *4*, 5339–5349.
  118. Sanson, C.; Schatz, C.; Meins, J.-F. L.; Soum, A.; Garanger, E.; Thévenot, J.; Lecommandoux, S. A Simple Method to Achieve High Doxorubicin Loading in Biodegradable Polymersome. *J. Controlled Release* **2010**, *147*, 428–435.
  119. Raikher, Y. L.; Stepanov, V. I. Absorption of AC Field Energy in a Suspension of Magnetic Dipoles. *J. Magn. Mater.* **2008**, *320*, 2692–2695.
  120. Fortin, J.-P.; Gazeau, F.; Wilhelm, C. Intracellular Heating of Living Cells Through Néel Relaxation of Magnetic Nanoparticles. *Eur. Biophys. J.* **2008**, *37*, 223–228.
  121. Trahms, L. Biomedical Applications of Magnetic Nanoparticles. In *Lecture Notes in Physics*; Odenbach, S., Ed.; Springer-Verlag: Heidelberg, 2009; Vol. 763, pp 327–358.
  122. Taking into account dilution effects, the overall iron oxide concentration in the sample is indeed 0.175 g/L. Using 0.07 W/g as the SLP value of the USPIOs under such a RF magnetic field and inferring adiabatic conditions, we expect a heat production of 0.18 J per hour. The mass of water to heat up being  $\sim 4$  g, we expected a temperature increase of only 0.01 °C/h.
  123. Dvolaitzky, M.; de Gennes, P.-G.; Guedeau-Boudeville, M.-A.; Jullien, L. A molecular drill?. *C. R. Acad. Sci. Paris Sér. II* **1993**, *316*, 1687–1690.
  124. Guedeau-Boudeville, M.-A.; Jullien, L.; di Meglio, J.-M. Drug Delivery: Piercing Vesicles by Their Adsorption onto a Porous Medium. *Proc. Natl. Acad. Sci. U.S.A.* **1995**, *92*, 9590–9592.
  125. Bernard, A.-L.; Guedeau-Boudeville, M.-A.; Marchi-Artzner, V.; Gulik-Krzywicki, T.; di Meglio, J.-M.; Jullien, L. Shear-Induced Permeation and Fusion of Lipid Vesicles. *J. Colloid Interface Sci.* **2005**, *287*, 298–306.
  126. Lenglet, J.; Bourdon, A.; Bacri, J.-C.; Demouchy, G. Thermomodiffusion in Magnetic Colloids Evidenced and Studied by Forced Rayleigh Scattering Experiments. *Phys. Rev. E* **2002**, *65*, 031408.
  127. Cotton, J.-P. In *Neutron, X-ray and Light Scattering*; Linder, P., Zemb, T., Eds.; North-Holland: Amsterdam, 1991; pp 3–31.
  128. Brûlet, A.; Lairez, D.; Lapp, A.; Cotton, J.-P. Improvement of Data Treatment in Small-Angle Neutron Scattering. *J. Appl. Crystallogr.* **2007**, *40*, 165–177.
  129. Hasmonay, E.; Dubois, E.; Bacri, J.-C.; Perzynski, R.; Raikher, Y. L.; Stepanov, V. I. Static Magneto-Optical Birefringence of Size-Sorted  $\gamma$ -Fe<sub>2</sub>O<sub>3</sub> nanoparticles. *Eur. Phys. J. B* **1998**, *5*, 859–867.
  130. Sbalzarini, I. F.; Koumoutsakos, P. Feature Point Tracking and Trajectory Analysis for Video Imaging in Cell Biology. *J. Struct. Biol.* **2005**, *151*, 182–195.
  131. Vasseur, S.; Duguet, E.; Portier, J.; Goglio, G.; Mornet, S.; Hadová, E.; Knížek, K.; Marysko, M.; Veverka, P.; Pollert, E. Lanthanum Manganese Perovskite Nanoparticles as Possible *In Vivo* Mediators for Magnetic Hyperthermia. *J. Magn. Mater.* **2006**, *302*, 315–320.
  132. Platil, A.; Tomek, J.; Kaspar, P. Characterization of Ferromagnetic Powders for Magnetopneumography and Other Applications. *Sensor Lett.* **2007**, *5*, 311–314.